Annual RPI report for FY 2019. Tasks 7, 8, and 9

Task 7: Hydrometeor Classification

7.1 Tornado Debris Signature (TDS)

In the past year, having validated the experiment automated TDS detection algorithm embedded within the Hydrometeor Classification Algorithm (HCA) and examined the nature of the false alarms, we have realized that the constraints inherent to the current HCA are too severe for acceptable TDS algorithm performance. As a result, we have opted to pursue an object-based TDS algorithm. Although this new object-based algorithm uses the TDS classifications produced by the experimental HCA, the actual output of the algorithm is an object or data table (similar to the TDA). The new algorithm identifies and extracts clusters of TDS classifications in the experimental HCA (i.e., "Preliminary Detections"), after which various characteristics (e.g., size, maximum aggregation value, and aspect ratio) for each TDS "cluster" are calculated. Those "clusters" that are highly non-circular, have comparatively low maximum aggregation value, and are relatively small are removed; the specific thresholds used at this time are based upon an analysis of a verification datasets resulting from a manual examination of TDS cases. The detections that meet these criteria are then deemed to be valid detections (e.g., "Final Detections"). One of the primary benefits of an object-based algorithm is that the TDS detections can be overlaid atop existing radar products that a meteorologist responsible for severe weather and tornado warnings would already be examining. This type of presentation allows someone familiar with radar data and severe storm conceptual models to quickly assess the viability of detection.

Additional cases in less climatologically favored regions for tornadoes (e.g., New York) were added to the validation dataset in FY19. Whereas the TDS-enabled HCA produced a false alarm rate of 82.5%, the additional, object-based thresholding reduces the FAR to ~19.6%; the number of false alarms drop from 1517 to 57, whereas the number of correct detections (i.e., "hits") drops 322 to 235. Attribution analysis for the false detections indicates that false detections in the TDS-enabled HCA are most commonly caused by ground clutter, gust fronts, and data quality-related issues in the Doppler velocity data (e.g., dealiasing errors, high-variance velocity estimates, etc.). When the thresholds are applied at the object level, the most common sources for false detections are hail contamination, high-variance velocity estimates, and gust fronts. The vast reduction in false detections indicates that the object-based algorithm is better able to automatically detect TDS events with many fewer false detections compared to the TDS-enabled HCA (Fig. 7.1.1).

A presentation summarizing development and assessment of the performance of an object-based tornado debris signature detection algorithm was made by J. Snyder at the 39th International Radar Conference in Japan (Snyder et al. 2019).

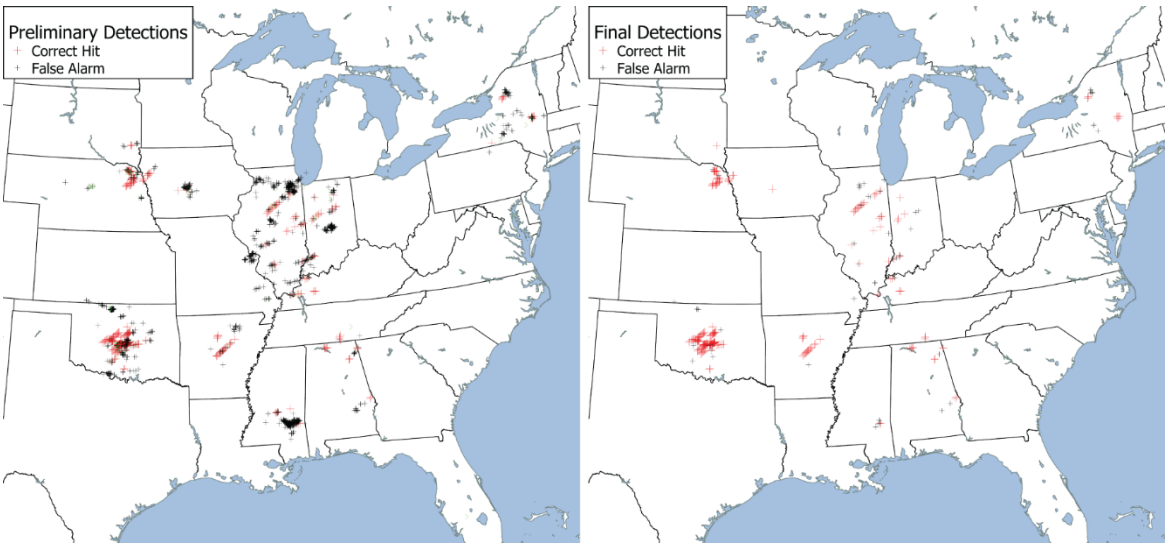

Fig. 7.1.1 Maps of the (left) preliminary detections from the TDS-enabled HCA and the (right) final detections from the object-based algorithm for the data used to validate the algorithm. In both panels, the black "+" signs indicate false detections and the red "+" signs indicate correct detections.

Task 7.2 Classification of winter precipitation

The spectral bin classifier (SBC) and the melting layer detection algorithm (MLDA) are the two primary modules of the modified winter surface classification algorithm (WsHCA). Our work on further modification and refinement of SBC and MLDA is described herein.

7.2.1 One-dimensional melting snow model and spectral bin classifier

Until recently, the classifier used as an input the vertical profiles of temperature and humidity from the HRRR model updated every hour and some generic size distribution of ice particles above the melting layer. The SBC classifier uses a Lagrangian one-dimensional melting snow model (1D-MS) developed at NSSL several years ago (Ryzhkov et al. 2014; Troemel et al. 2014; Reeves et al. 2016). The 1D-MS is a Python-based Lagrangian spectral bin model coupled to a polarimetric radar operator (Ryzhkov et al. 2011). Flux conservation is assumed, with one snow particle above the melting layer equaling one rain drop below the melting layer (i.e., aggregation and breakup are excluded). The environment can be specified using an idealized environment or from observed sounding data. Treatment of various degrees of riming is included, from unrimed snow aggregates to heavily-rimed particles. A number of updates have been made since the original model formulation. An explicit treatment of the mass transfer due to of evaporation and sublimation is now included. In addition, environmental feedbacks due to microphysical processes have been added for both temperature and moisture, allowing the environment to evolve in response to the precipitation. Previous versions specified a rain size distribution at the surface and extrapolated this to a snow distribution above the melting level. The current version

allows for the direct specification of a snow size distribution above the melting level, which can be estimated from radar data (e.g., Ryzhkov and Zrnić 2019) and does not require evaporative losses to be neglected as is done when specifying particle size distributions at the surface and extrapolating upward. Radar scattering calculations are performed using the PyTMatrix package (Leinonen 2014), with support for Ku, Ka, X, C, and S bands included. Numerous approaches for calculating the effective relative permittivity of particles is included (including all topology combinations of the Maxwell-Garnett and Polder-van Santen methods), and with a new formulation for melting snow that attempts to incorporate the initial internal soaking of meltwater.

Work is ongoing to continue to extend the 1D-MS. The model is being re-written in an object-oriented approach to make the code more readable and user-friendly, and formal online documentation is being prepared to guide users on how to use the model for easier sharing with research partners. In addition, a simple parameterization for accretion following Trömel et al. (2014) is being implemented. Finally, efforts are underway to make the model more comprehensive by adding the treatment of pristine ice crystals with adaptive habit depositional growth following Chen and Lamb (1994) and Jensen and Harrington (2015) to allow for the investigation of, for example, local generation of needles in a refreezing layer.

7.2.2 Summary of recent changes to SBC

(a) Changes to software engineering

In the third quarter of 2018-2019, Jacob Carlin and John Krause undertook the rewriting and streamlining of the SBC code. The SBC code has been through several different platforms and has been used by a number of different scientists since its introduction in 2014. As such, it was difficult to know which parameters and variables had been added or removed over time. To facilitate this, Jacob created a flow chart of the now named SBCv2 and list of all of the modifications to this C++ code base that we made as we progressed. As with any rewrite, several formulae were evaluated and changed as well as some modifications to the logic to speed up the computations and to reduce the memory footprint, which had grown over time. In the end, John was able to create a piece of code that can compare SBCv1, SBCv2, and the current SBCv3 code bases from a single input. The SBCv3 code improves over the SBCv2 with an 8x faster execution time and 10x lower memory requirement for a CONUS US HRRR output. This is a significant improvement. We also have a flowchart of the logic and list of modifications applied from v2->v3. Finally, Jacob has been able to work with this code natively and run it on several cases.

(b) Changes to classification scheme

Most of the classification scheme has remained the same. However, we implemented a new wetbulb-based “pre-classification” scheme for obvious snow (SN), rain (RA), and freezing rain

(FZRA) classifications that skips the model microphysical processes and significantly speeds up the code. We also added a logic split for cases of liquid nucleation at cloud top and subsequent nucleation/freezing beneath it.

(c) Changes to model physics/parameters

We have begun expanding the number of microphysical processes that are included in the SBC. Primarily, we implemented an explicit calculation of evaporation. This allows for the variable effects of evaporation on different particle size bins, and eliminates the need to assume a saturated wetbulb temperature profile as done previously. Preliminary results suggest modest impacts for the default particle size distribution (PSD) and number of size bins, but more substantial impacts for PSDs featuring a large number of small particles (Fig. 7.2.1). In the latter case, changes include both transitions toward more ice due to evaporation of liquid water (e.g., FZRA→FZRAPL, FZRAPL→PL) and toward more water due to condensation on melting/melted particles (e.g., IP→FZRAPL, FZRAPL→FZRA). Recall that abbreviation PL stands for ice pellets and FZRAPL for a mixture of freezing rain and ice pellets.

In addition, we are investigating the impact of a number of other potential changes, namely the number of particle size bins, the assumed PSD, and the vertical resolution around the 0˚C wetbulb level. The impact of each of these changes is related to the other conditions (e.g., the aforementioned impact of evaporation based on number of bins and PSD). In general, increasing the number of size bins and varying the input PSD can significantly affect the resultant classifications in transition regions. For the same PSD, increasing the number of size bins results in movement toward more mixed regions (e.g., PL, FZRA → FZRAPL, RA → RASN, RAPL, etc. where RASN stands for a mixture of rain and snow or wet snow). For the same number of size bins, how skewed the PSD is toward small or large particles can strongly affect the ratios of ice and water at the surface used to classify the precipitation type. Super-sampling near the 0C level appears to be important as well (Fig. 7.2.2): assuming the conditions at the bottom of a layer apply over the full depth of the layer will generally result in overly-rapid melting and refreezing, whereas linearly interpolating to a higher resolution allows for a more gradual melting/refreezing process.

7.2.3 Verification of the SBC performance

Much of our attention has been on developing a consistent and objective verification methodology to discern the impacts of various proposed changes quantitatively. We are using data from both mPING and manned ASOS stations to validate the SBC, and consider multiple potential “hits” for mixed reports (i.e., reports of either PL or FZRA validate an FZRAPL classification). Given the heterogeneous and scattered nature of observations, point-by-point validation can obfuscate the impact of modifications. Of particular interest is developing a verification methodology that considers different degrees of wrongness, as might be relevant to operational forecasters using the SBC (i.e., predicting RA instead of SN is a worse forecast than

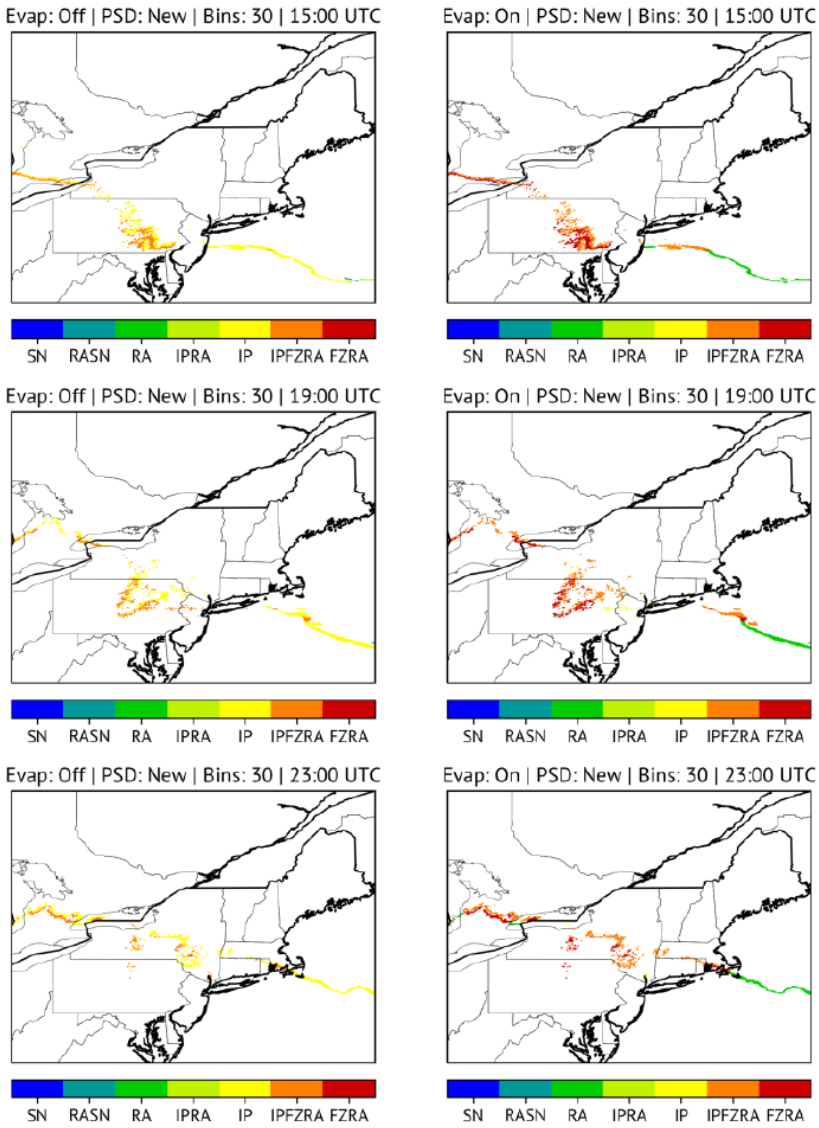

Fig. 7.2.1 Classification (left) without evaporation and (right) with evaporation for an adjusted PSD and 30 size bins for three different times on 12 February 2019.

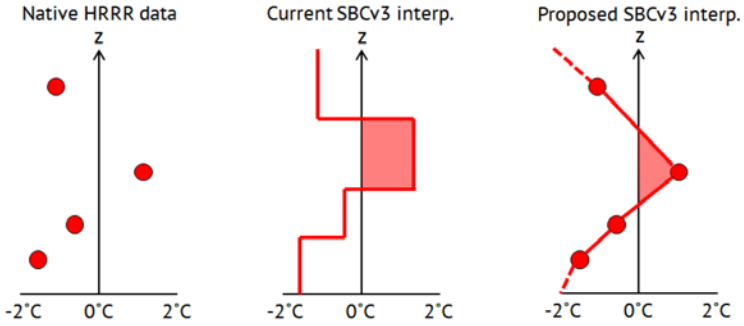

Fig. 7.2.2 Visual representation of the (left) native HRRR data points, (middle) the current translation of HRRR data points to layers, and (right) the result of super-sampling near 0°C.

predicting FZRAPL instead of PL). One approach for accomplishing this is a distance-based method where the metric we seek to minimize is the distance to the nearest correct observation. Vector maps were created with vectors indicating the direction of the nearest correct observation scaled by the distance in order to reveal systematic biases in the SBC classification and HRRR model data. We have recently begun exploring a "cost function" approach, in which observations are spread isotropically in space and weighted by type and linearly in time and space out to some maximum distance (Fig. 7.2.3). This allows for the probability of each precipitation type at each grid point (where observational data exists) as an estimate of confidence and contribution to the cost function. Using HRRR analysis temperature fields as bulk proxies for precipitation type, this method can reveal where there is a systematic bias in the HRRR data (e.g., the advance of IP northward; Fig. 7.2.3) or local effects that are not captured by the bulk SBC classifications (e.g., local generation of snow in the Appalachians; Fig. 7.2.3).

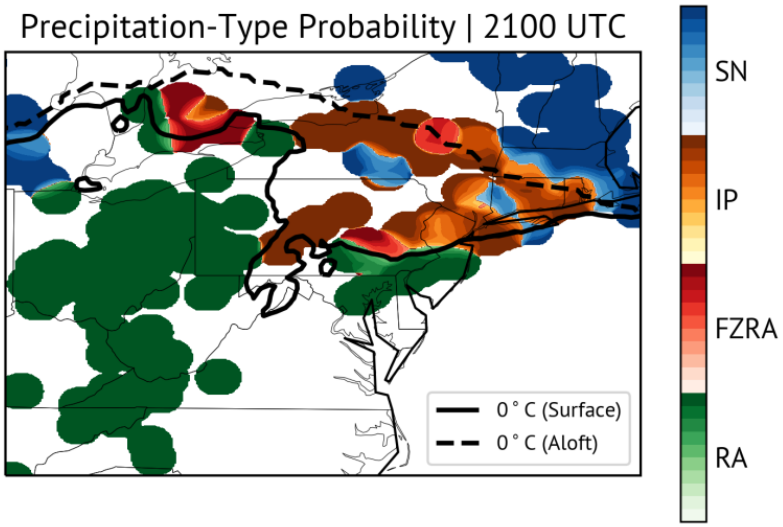

Fig. 7.2.3 Normalized maximum probability precipitation type at 2100 UTC on 12 Feb 2019. The surface 0C line and 0C line aloft (anywhere in the column) from the HRRR analysis are shown as proxies for where rain, snow, and mixed-phase precipitation should occur.

Excellent opportunity to verify the SBC performance comes from our partnership with Korea Meteorological Agency (KMA) and Kyungpook National University of Korea through participation in the International Collaborative Experiments for Pyeongchang 2018 Olympic and Paralimpic winter games (ICE-POP). Alexander Ryzhkov serves on the Advisory Board of ICE-POP. A unique dataset obtained from the measurements by ground and remote sensing instruments (including polarimetric radars) has been obtained during the Winter Olympics in Pyeongchang. We shared our SBC classifier with our Korean partners and hosted two graduate students from Korea in January 2018. The SBC classifier was utilized for several transitional winter events during the Olympics and beyond. The classification results have been presented at the 39th International Conference on Radar Meteorology in a joint paper by Bang et al. (2019). It

is demonstrated that the SBC exhibits superior performance compared to other four operational algorithms used by KMA for classification of winter precipitation. We plan to provide an overview of these results at the ROC DQ meeting in December 2019.

7.2.4 MLDA development

7.2.4.1 Sidelobe contamination impact on MLDA

Occasional failures of MLDA can be attributed to ground clutter or sidelobe contamination. On the request from the ROC Application Branch (Engineering Change Proposal (ECP) 0089), John Krause examined 18 cold season events with compromised results of MLDA. After analysis of about 85 hours of data, it was found that the melting layer (ML) was not identified in 2 cases for which WsHCA correctly classified precipitation at the surface as snow. Examination of remaining 16 events reveals two primary reasons for the contamination of the MLDA output. First, antenna sidelobes near the radar that interact with ground clutter can lower the values of the cross-correlation coefficient ρ_{hv} in the first 10 range gates. Second, excessive Doppler filtering of the radar signal along the Doppler velocity zero isodops causes reduction of ρ_{hv} which can be misinterpreted as the ML signature. If the sidelobe clutter becomes widespread and persistent in regions of weak meteorological radar echoes, these reduced values of ρ_{hv} can overwhelm the statistics to determine the melting layer bottom. The outcome is that the ML bottom appears to the too low and close to the radar. Sidelobe contamination signatures often look like an arc of low ρ_{hv} near the radar. In all examined cases, the best solution was to limit the input data to MLDA to locations further away from the radar. A good solution might include the use of sounding or NWP model to determine a 2-km-deep layer containing ML or reasonable trimming of the closest range gates to suppress sidelobe contamination. John Krause's analysis demonstrates that removing only the first two gates from the computation eliminates almost 80% of the errors.

7.2.4.2 Novel concept of melting layer detection and determination of its parameters

A novel concept of the melting layer detection and determination of its top and bottom heights is introduced by Ryzhkov et al. (2019). It utilizes large statistics of the "intrinsic" vertical profiles of polarimetric radar variables through the ML obtained with the use of the QVP methodology. The statistical correlations between intrinsic vertical profiles of Z and ρ_{hv} in the melting layer are of particular importance. Another important component of the method is simulation of a multitude of the model radial profiles of Z and ρ_{hv} at all antenna tilts for different heights and strengths of the ML and storing them in lookup tables. These radial profiles are generated taking into account the antenna pattern and the impact of beam broadening at longer distances from the radar. Two important parameters of the radial profiles of ρ_{hv} are the range where ρ_{hv} starts decreasing due to beam interception of the bottom of the ML and the "strength" of the ρ_{hv} minima associated with the ML. The "intrinsic" top and bottom of the ML are determined by finding the best match between the model and observed radial profiles of ρ_{hv}. The

matching routine is illustrated in Fig. 7.2.4 where the model and measured radial profiles of ρ_{hv} at elevation 1.45° are compared.

The distances r_b where both model and measured ρ_{hv} as well as the "strength" of the ML defined as

$$S = \int_{r_b}^{r_t} [\rho_{hv}^{(th)} - \rho_{hv}(r)]\, dr \qquad (7.1)$$

are matched are used to pick up an appropriate model vertical profile of the ML with its "true" heights of the top and bottom. In the example in Fig. 7.2.4, the ρ_{hv} threshold $\rho_{hv}^{(th)}$ is equal to 0.985.

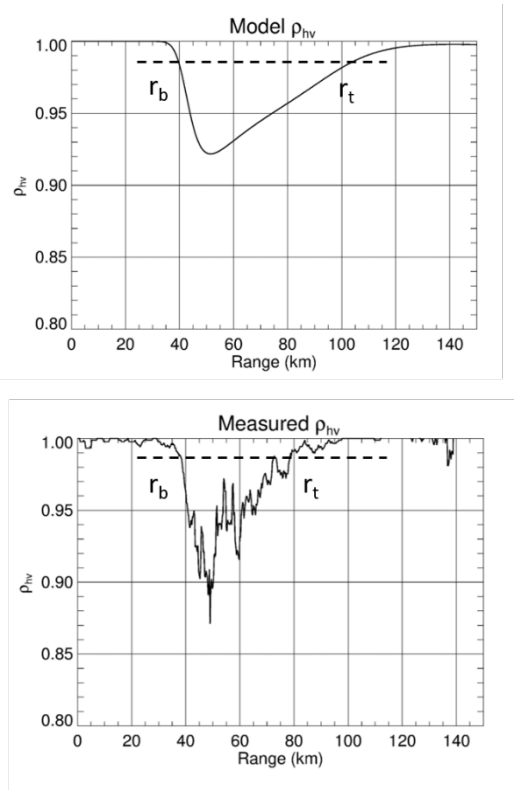

Fig. 7.2.4 Simulated and measured radial profiles of ρ_{hv} used for a matching routine for determination of the parameters of the ML.

An example of PPI of Z and ρ_{hv} at El = 1.45° for the winter storm observed by the KICT WSR-88D radar is shown in Fig. 7.2.5. The range to the ML bottom r_b and the corresponding ML bottom height as functions of azimuth are displayed in Fig. 7.2.6. Note that azimuthal dependency of the

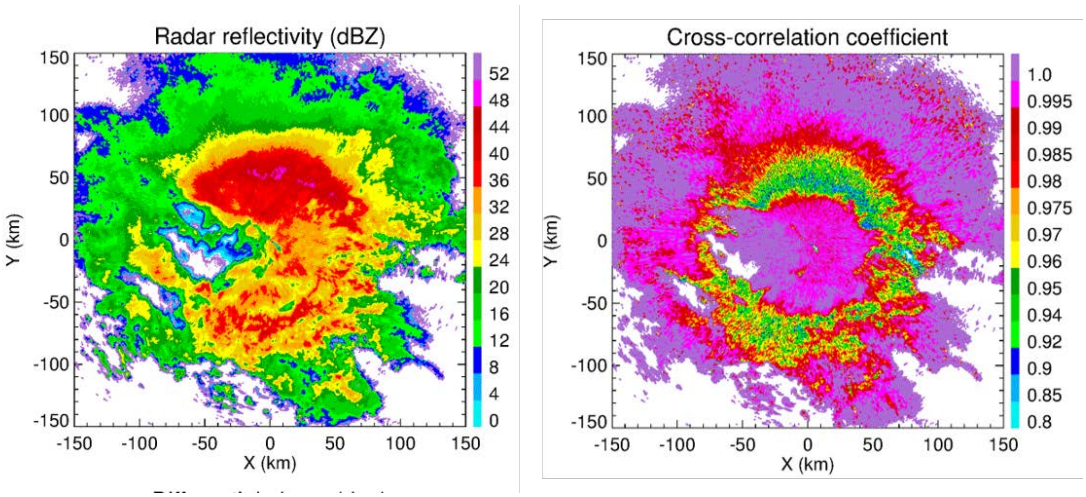

Fig. 7.2.5 PPIs of Z and ρ_{hv} at El = 1.45° for the storm observed by the KICT WSR-88D radar on 2011/12/19.

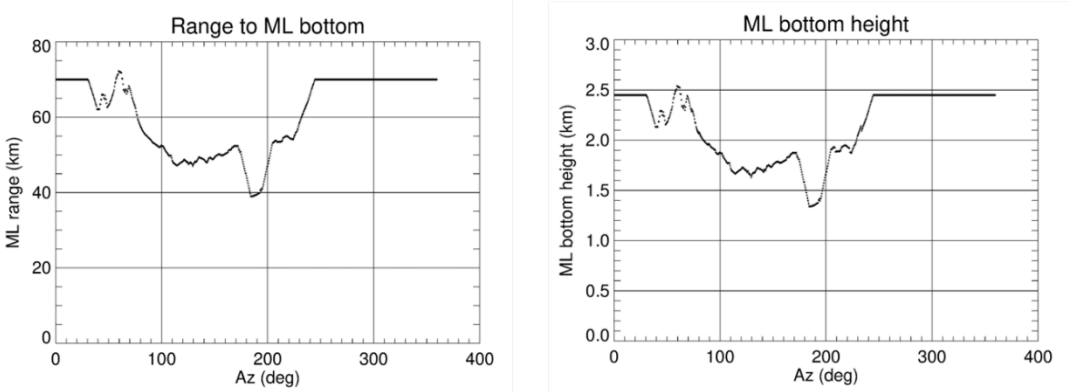

Fig. 7.2.6 Azimuthal dependencies of the distance to the ML bottom and ML bottom height for the case illustrated in Fig. 7.2.4.

ML bottom height is well captured by the algorithm and the estimate of this height is not affected by antenna beam broadening. Repeating the procedure at multiple elevation angles would produce the estimates of the ML bottom and top at different distances from the radar. Therefore, both azimuthal and radial dependencies of the parameters of the ML can be quantified using the suggested technique. In 2019, the major principle of a new MLDA method was outlined and tested for only two cases of stratiform rain with low bright band. Further testing and development of the algorithm will follow in FY2020.

The proposed methodology hinges on the accurate characterization of the intrinsic vertical profiles of Z and ρ_{hv} within the melting layer and their statistical correlations. This was done in the two comprehensive statistical studies of the ML QVPs – one at CIMMS/NSSL (Griffin et al. 2019) and another in Germany (Troemel et al. 2019) in close partnership with CIMMS/NSSL. Composite histograms of different radar parameters within the melting layer measured at S band are presented in Fig. 7.2.7. Correlations between minimal value of ρ_{hv} and maximal value of Z_{DR} within the ML with its depth and strength in terms of Z enhancement are illustrated in Fig. 7.2.8.

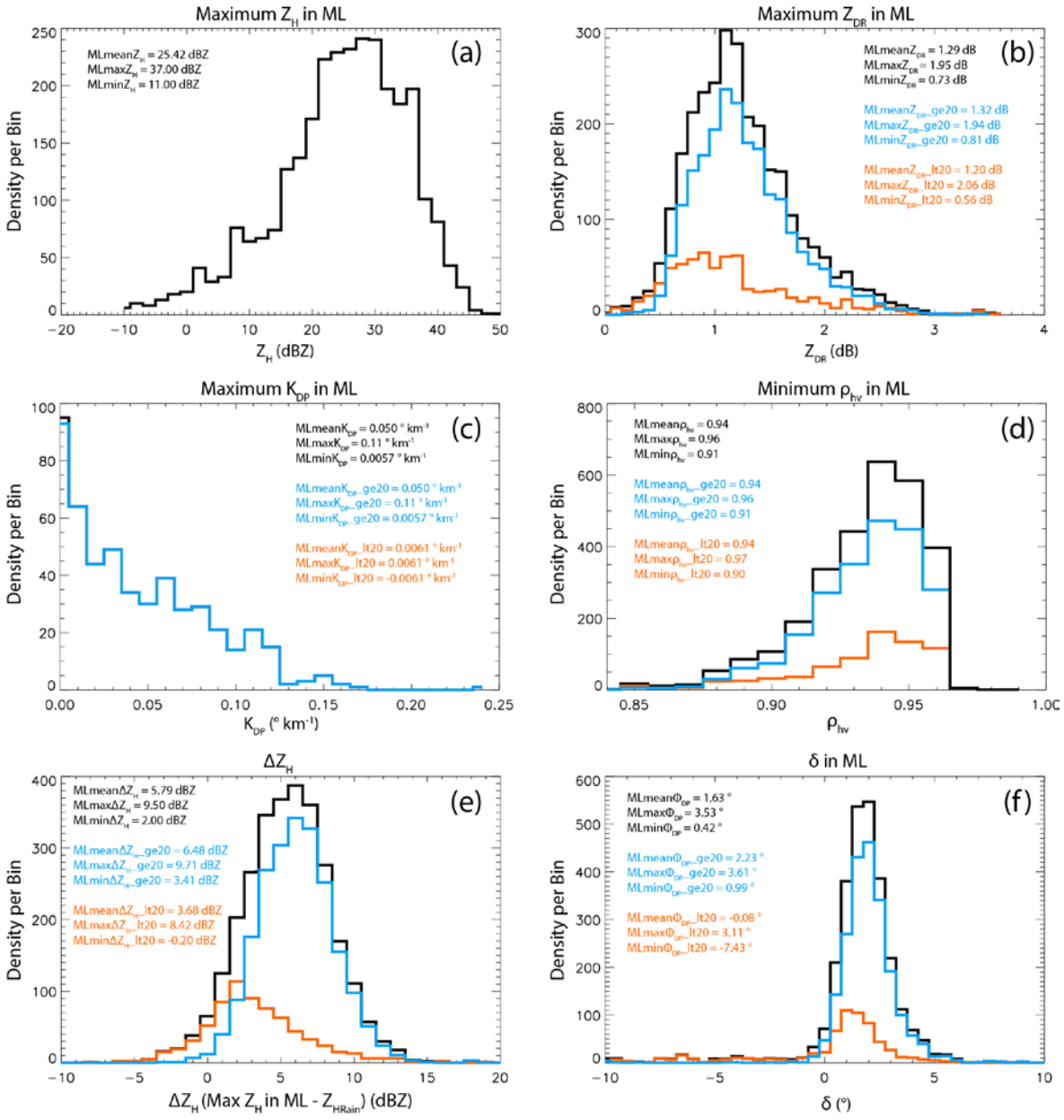

Fig. 7.2.7 Composite histograms of a) maximum Z_H in the ML (dBZ), b) maximum Z_{DR} in the ML (dB), c) maximum K_{DP} in the ML (° km^{-1}), d) minimum ρ_{hv} in the ML, e) ΔZ_H (i.e., Z_H in ML - Z_H in rain; dBZ), and f) δ (°) in the ML, for the 33 QVP ML events. Mean, 90th percentile maximum (indicated as max), and 10th percentile minimum (indicated as min) values of the variables are indicated in each panel, for the total dataset (represented by the bold black lines), the data corresponding to Z_H < 20 dBZ (represented by the orange lines), and the data corresponding to $Z_H \geq 20$ dBZ (represented by the blue lines). From Griffin et al. (2019).

The correlation dependencies involving min(ρ_{hv}) are used for designing our new technique for determination of the parameters of the ML and polarimetric vertical profile of reflectivity (PVPR) technique which is briefly described under the task 8.2 of this report.

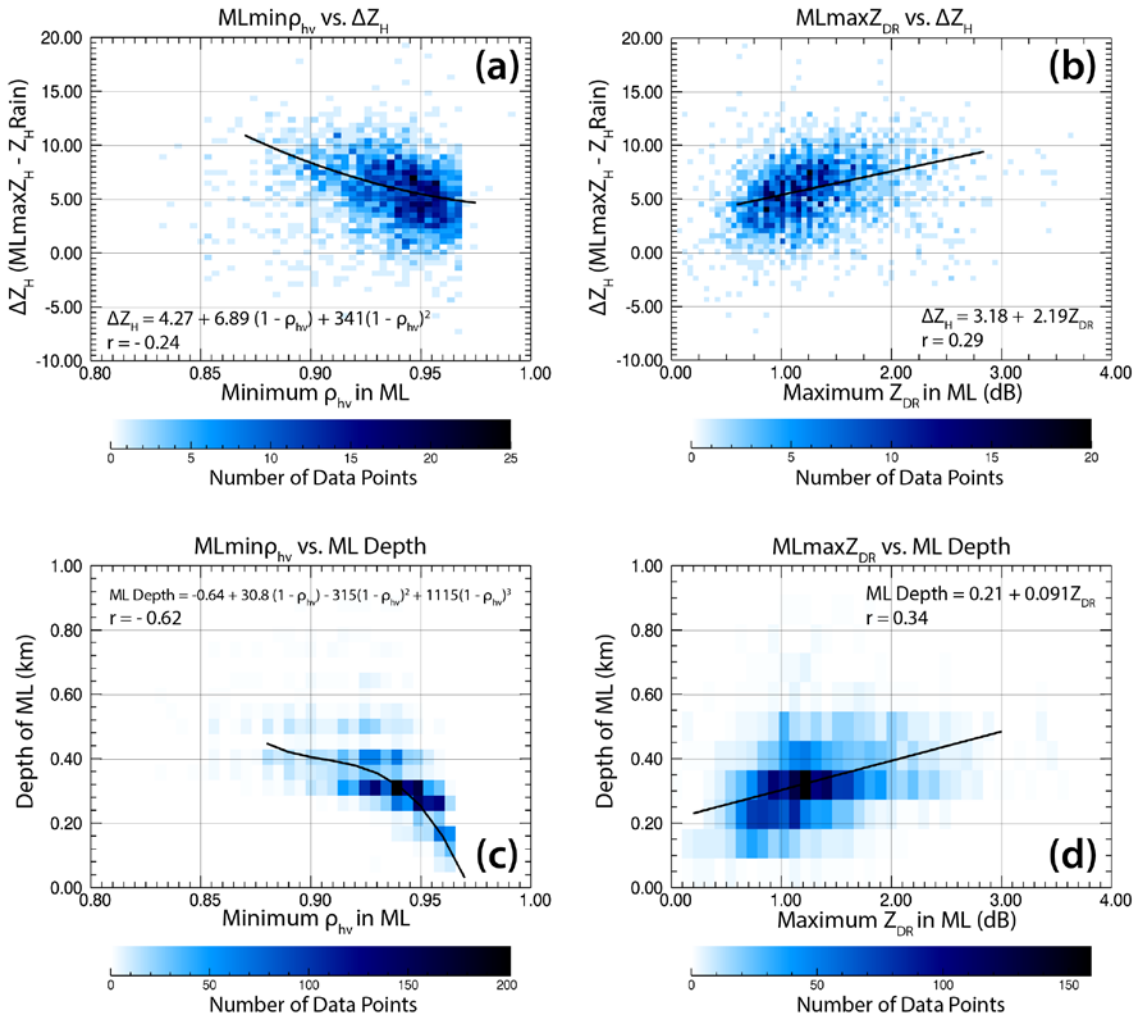

Fig. 7.2.8. Composite density scatterplots of a) minimum ρ_{hv} in the ML vs. ΔZ_H (dBZ), b) maximum Z_{DR} in the ML (dB) vs. ΔZ_H, c) minimum ρ_{hv} in the ML vs. ML depth (km), and d) maximum Z_{DR} in the ML vs. ML depth, for the 33 QVP ML events. Note: ΔZ_H = (maximum Z_H in the ML) – (Z_H in rain). Correlation between the variables (i.e., r) is indicated for the data fit in each plot. From Griffin et al. (2019).

Task 7.3 Identifying Areas and Sources of Reduced Radar Data Quality

Poor data quality and "artifacts" in the data (to include returns for which the signal is not a valid representation of the meteorological scatterers in the radar volume) can reduce the performance of various algorithms (e.g., HCA and QPE) and complicate users' subjective analysis of the radar data. In FY19, we developed preliminary algorithms to identify the three-body scatter signature/spike (TBSS, a.k.a., "hail spike") and non-uniform beam filling (NBF) and a simple yet effective way to identify ground clutter that remains after the use of existing clutter suppression scheme(s).

The TBSS algorithm was implemented following Mahale et al. (2014). It adapts the fuzzy logic-based HCA to locate and identify locations of multipath scattering that can occur as the radar beam is redirected to the ground upon being scattered by hailstones aloft. To do this, the algorithm first locates HCA classifications of large or giant hail and then applies a specific fuzzy logic scheme down radial of the hail to determine if it is contaminated by TBSS. Observed TBSS contamination can often extend down radial from the initial point, and the algorithm allows TBSS detections to continue if the gates fall within the fuzzy logic parameters. The TBSS algorithm, since it uses the existing HCA as a "first guess" to locate hail, cannot be run within the existing HCA without modification. An example of the TBSS-enabled HCA is shown in Fig. 7.3.1.

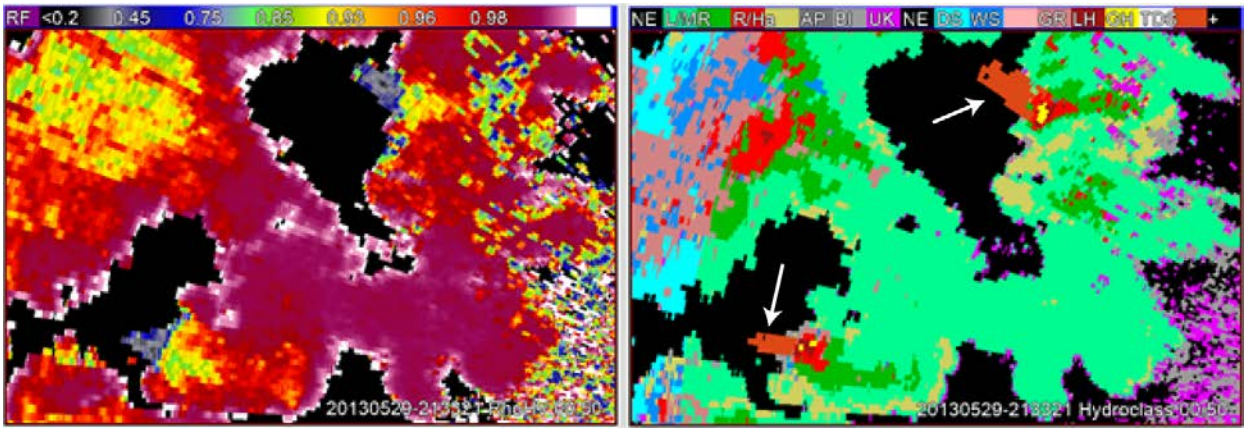

Fig. 7.3.1. An example of (left) ρ_{hv} and (right) TBSS-enabled HCA. The white arrows in the right panel point to prominent TBSSs.

The TBSS detection performs well except in areas of NBF and ground clutter. NBF lowers ρ_{hv} values downstream of origination, which can create long false streaks of TBSS. Ways to mitigate such false detections are being examined. For example, a simple way to mitigate NBF-related TBSS false detections would be to limit the TBSS detection to a maximum number of gates. The false positive error would still be present, but it would be contained. Another option would be to limit the TBSS detections in regions of NBF. This option would probably create several locations where missed detections of TBSS would exist. NBF can be caused by the same hail cores that produce a TBSS, though severe NBF can increase the difficulty in identifying a TBSS.

NBF detection is based on an examination of vertical and horizontal gradients in Φ_{DP}. The method computes the ρ_{hv} reduction factor as described in Ryzhkov and Zrnić (2019, pp 189-192). However, the maximum reduction is often found near but not co-located with the drop in ρ_{hv} which is often observed in the data as streaks of lowered ρ_{hv}. The ρ_{hv} reduction factor is computed with both a vertical and horizontal gradient of Φ_{DP}. As the gradient is computed through the high point of the value, the gradient will go to zero and then reverse sign, leaving the highest gradients near but not at the highest maximum values of Φ_{DP} as computed across (not

along) radials. Although the reduction factor is an interesting standalone product, we felt that it would be better to utilize it to identify those locations in the ρ_{hv} field that could be suspected of being contaminated by NBF. Meteorologists often see these areas as streaks of reduced ρ_{hv} along the radial. To do this we first smoothed the ρ_{hv} along the radial with a 7 gate median filter. Then we looked for regions that had both low ρ_{hv} (< 0.97) and a significant ρ_{hv} reduction factor (< 0.96) nearby (3 gates). These locations were flagged as contaminated by NBF (the upper right panel in Fig. 7.3.2).

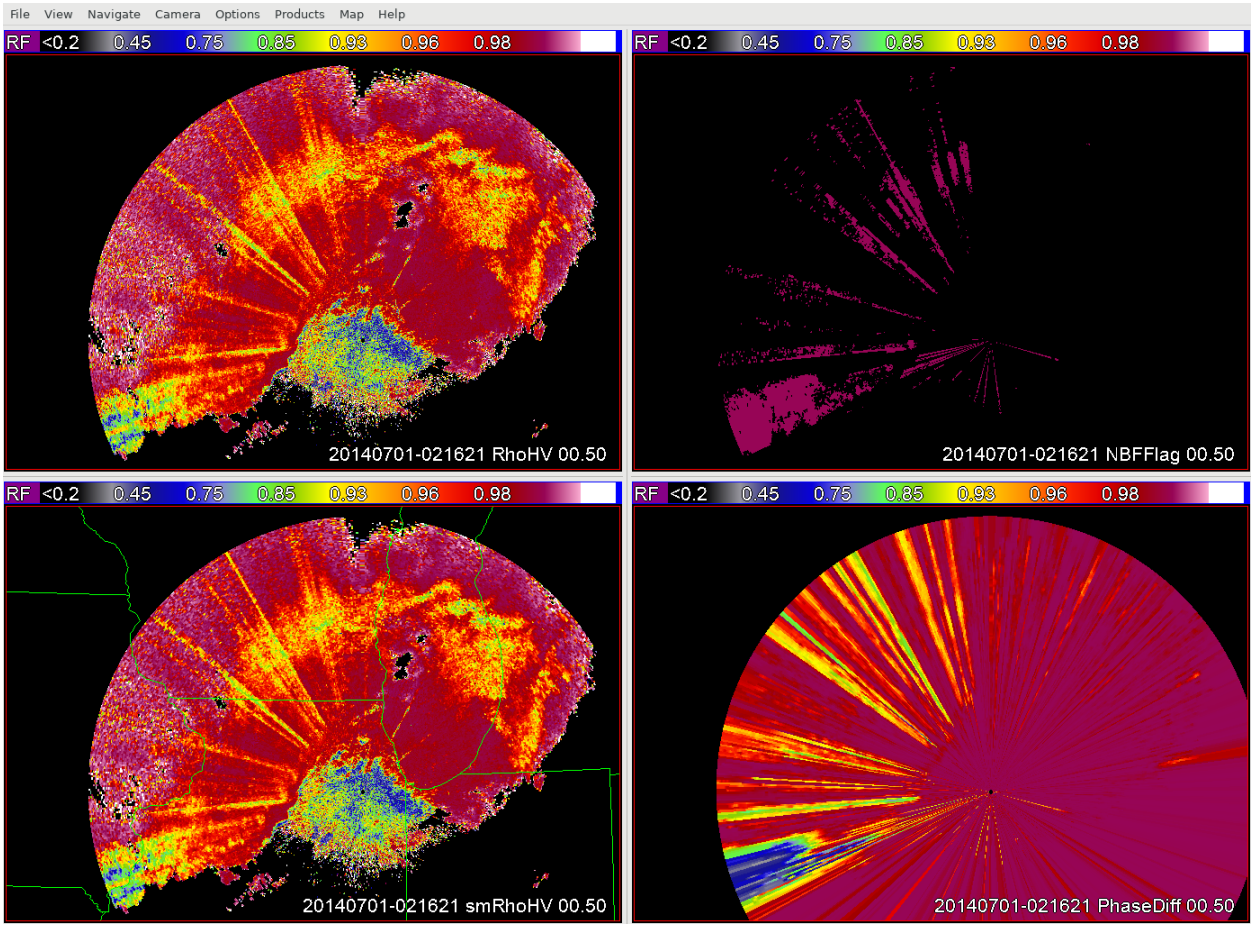

Fig. 7.3.2. (Upper left) measured ρ_{hv}, (lower left) smoothed ρ_{hv}, (upper right) the NBF flag, and (lower right) estimated ρ_{hv} reduction owing to the Φ_{DP} gradient. Data are from the KLOT radar on 1 July 2014.

Finally, although the existing ground clutter suppression schemes can remove a substantial amount of stationary ground clutter, they generally have difficulties removing clutter from wind farms, largely owing to the non-zero radial velocity characterizing wind farm clutter. Clutter from wind farms can produce errors in the HCA and other algorithms. For example, both the TDS-enabled HCA and the current operational HCA can overclassify hail and TDS when convective storms are near wind farms. To mitigate this issue, the long-term average reflectivity (LTAR) product is used. Because meteorological echoes tend to be transient compared to ground

clutter sources, their impact on the long-term reflectivity is relatively small. Consequently, an average of ~1 month of reflectivity data tends to highlight only persistent clutter like power lines, terrain features, and, relevant for this discussion, wind farms. An experimental version of the HCA uses the LTAR data to mask HCA output where LTAR exceeds some value (in the case of Fig. 7.3.3, the HCA data are masked where LTAR exceeds ~15 dBZ).

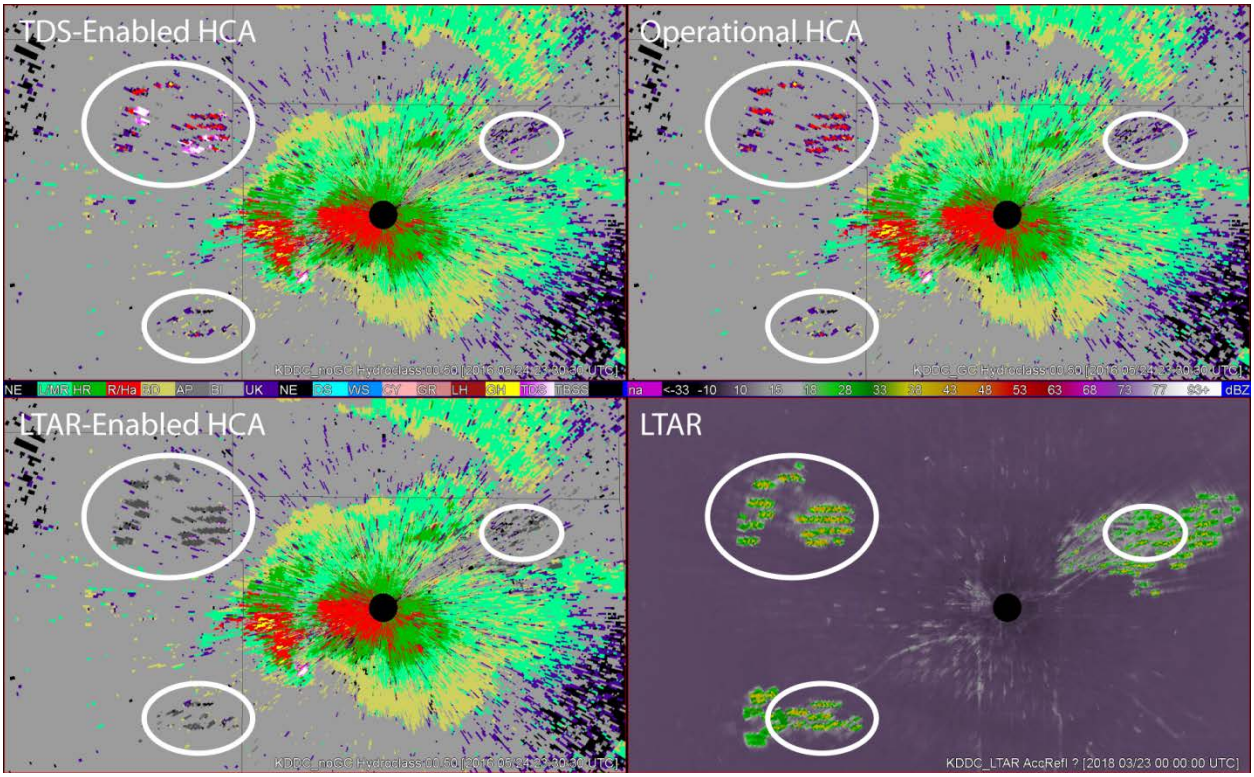

Fig. 7.3.3. Clockwise from the upper-left, output of the TDS-enabled HCA, the current operational HCA, the experimental LTAR-enabled HCA, and LTAR. In the LTAR-enabled HCA, locations characterized by LTAR exceeding ~15 dBZ are denoted by the dark gray color. The white ovals highlight the three main areas where wind farm clutter produced erroneous HCA output that is suppressed in the LTAR-enabled HCA. Red and yellow colors in the HCA products denote hail; the pink and white colors in the TDS-enabled HCA denote TDS. All in all panels, purple denotes the "unknown" category.

All codes for the above algorithms are deliverable upon request. A combined product of the three different types of reduced radar data quality was not created due to the order in which the data are needed. LTAR data are needed first to reduce hail detection errors from locations with wind farms. The NBF data are then needed to reduce erroneous hail reports found down radial of storm cores. Finally, TBSS can now be more accurately run because the HCA is not producing erroneous hail reports over wind farms or regions of NBF. The LTAR code is available as a AWS machine with scripts and output as a netcdf file. The code itself is a simple average of reflectivity data, but it requires the AWS system to run a month of data. This AWS process can

run any radar data in the Big Data Archive for any time frame. We used a month or 30 calendar days to generate the LTAR data used in the report. The NBF detection algorithm is a standalone C++ program that ingests a 3D volume of differential phase (Φ_{DP}) data to compute the Φ_{DP} difference between two different elevation cuts. Finally, the TBSS code is an HCA plugin that runs after both the HCA and the Hail Plugin. This implies ingesting radar data and the HCA output and modifying the HCA where TBSS signatures are detected.

8.1. Identifying Features in Convective Storms

The existing HCA and Hail Size Discrimination Algorithm (HSDA) rely upon the specific values of the radar variables at each location with no knowledge of the surrounding data. In other words, the HSDA result at some range gate depends only upon the values of Z, Z_{DR}, and other quantities at that location. In designing the HSDA, Ryzhkov et al. (2013) had to make certain assumptions about the characteristics of large (1"-2" diameter) and giant (2"+ diameter) hail. For example, it was assumed that giant hail is characterized by very high Z. However, we have seen cases in which very prominent size sorting has produced an anomalous size distribution characterized by an extremely low number concentration of very large hailstones, the result of which is only low or moderate Z (e.g., 30-40 dBZ). In such cases, the HSDA and HCA fail to detect the giant hail.

To better quantify some of the polarimetric characteristics of large and giant hail, hail reports from 13 giant-hail-producing storms were examined, and the location and time of hail reports (from the Storm Events Database) were matched to the nearest base-scan (0.5° elevation angle) data. A total of 110 giant hail reports and 189 large hail reports were included in this analysis. In the left panel of Fig. 8.1.1, the Z- Z_{DR} characteristics of the reported hail are plotted, where the

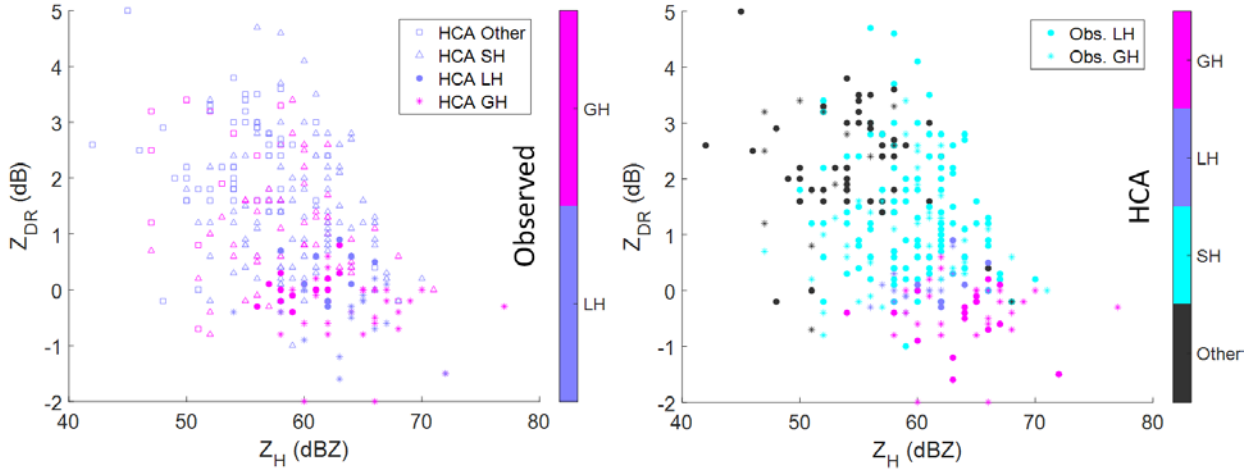

Fig. 8.1.1. Z- Z_{DR} scatterplots associated with the nearest range gate from 299 large and giant hail reports covering 13 cases. The points are the same in each panel, but the left panel shows the points colored by the observed hail class with the symbol denoting the HCA class, whereas the right panel shows the points colored by the HCA class with the symbol denoting the observed hail size class.

colors represent the observed size (pink for giant and purple of large), and the shape of the marker representing the HCA classification. As can be seen, there is not a readily apparent separation between the *observed* hail size classes (i.e., the pink and purple observed classes have significant overlap). The right panel of Fig. 8.1.2 shows the same data but with colors representing the HCA class at each report location/time and the shape representing the observed hail size class. The HCA, by design, tends to classify the high Z – low Z_{DR} data as giant hail, with large and small hail becoming more common as Z decreases and Z_{DR} increases. Note again, though, that the characteristics of large and giant hail overlap across much of the Z- Z_{DR} space – the clean distinction seen in the HCA results are not apparent in the observations from this limited set of cases.

Conceptually, we expect the largest hailstones to fall near and downstream of the updraft of convective storms (where such hailstones tend to grow). If there is significant overlap in the local radar characteristics of large and giant hail, then it is plausible to suggest that the hail size algorithms (such as the HSDA/HCA) should incorporate storm-scale feature information as well. In particular, we suspect that the HSDA can be improved by incorporating information about the location and intensity of the updraft. To provide a basis for this, the locations of the hail reports previously mentioned were examined relative to the center of the updraft (determined by conventionally used signatures such as the bounded weak echo region and Z_{DR} column; Fig. 8.1.2).

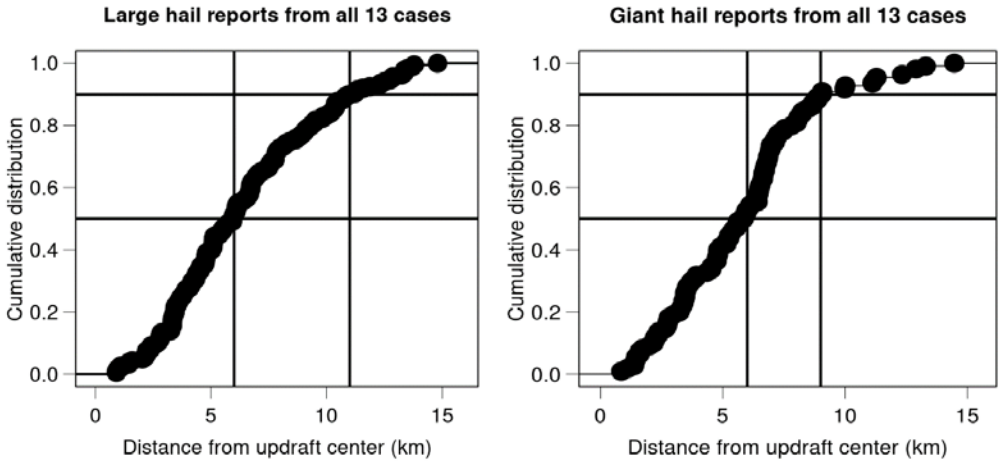

Fig. 8.1.2. The cumulative distribution of (left) large and (right) giant hail reports from the center of the updraft. The horizontal lines highlight the median (50th percentile) and 90th percentile values.

Although the median distance of large and giant hailstones from the updraft center was similar (~5.5 km), the occurrence of giant hail dropped off more frequently with distance compared to that of large hail. In particular, the 90th percentile for giant hail was ~9.5 km from updraft center, whereas it was ~10.5 km for the large hail reports. Regardless, almost all hail

reports examined fell within 15 km of the updraft, potentially providing a basis for including spatial information into the HCA.

Note only do we seek to use spatial information to improve the HSDA (by moving beyond the 1-dimensional nature of the HCA), but we also are striving to identify hail growth by examining polarimetric features aloft. As noted in previous reports, we have reason to think that mid-storm signatures such as highly negative Z_{DR} and low ρ_{hv} aloft may provide useful information on the location of large hail and its growth. We are currently creating a system with which we can examine products that may be valuable for identifying hail aloft (e.g., minimum Z_{DR} and ρ_{hv} at -20° C), though we have experienced non-trivial issues trying to create a cell-tracking method to extract the radar data that we want to study.

A good candidate for such cell-tracking method is the Multi-Cell Identification and Tracking (MCIT) algorithm that has been recently developed at CIMMS / NSSL (Hu et al. 2019). MCIT uses the "watershed" principle formulated in the original paper by Rosenfeld (1987). The advantage of the watershed methodology is that it is capable to identify and track cells for both isolated and clustered cloud systems. As opposed to many other tracking techniques, this methodology takes into account possible splitting and merging of individual cells.

Identification of a cell is performed based on the radar reflectivity Z data that are converted from the polar to Cartesian grid with horizontal resolution of 0.5 km and vertical resolution of 0.3 km. The parameter called Vertically Integrated Liquid (VIL) is computed in every 0.5 x 0.5 km pixel from the vertical profile of Z as

$$\mathrm{VIL} = \int_{H_b}^{H_t} \mathrm{M(h)\,dh} \qquad (8.1)$$

where mass water content M is estimated from radar reflectivity factor Z as

$$\mathrm{M} = 3.44\,10^{-3}\,\mathrm{Z}^{4/7} \quad , \qquad (8.2)$$

H_b and H_t are the heights of the bottom and the top of the cloud (Greene and Clark 1972). In (8.1) – (8.2), Z is expressed in mm^6m^{-3}, and M is in g/m^3. VIL is usually measured in kg/m^2 and varies between 0 and 70 kg/m^2. For VIL exceeding 50 kg/m^2 the storm potentially contains hail.

A cell peak is defined as a local maximum of VIL (or LVIL = 10 log(VIL)) within a radar echo that is at least 5 grid boxes in size in order to avoid noise and over-identification of cells. Two neighboring cells may appear to overlap but are still considered distinct as long as their maxima in terms of LVIL are separated by a valley that is at least 2 dB lower than the weaker of the two maxima. For each peak of VIL, the watershed routine determines a "watershed" area surrounding the peak with the boundary defined by a minimal VIL (see Fig. 4). The MCIT algorithm is written in MATLAB which offers a "watershed" function. The command used is simply "watershed (input, options)". These watershed areas surrounding VIL peaks are called "cells" and tagged with numbers.

Cell tracking is performed by a comparison of the VIL maps with identified cells at the two successive radar scans, e.g., scan n and scan n+1. Such comparison is done by shifting VIL map at scan n+1 back to the scan n using a shifting vector **ΔR.** At the beginning of a tracking process, **ΔR** = **U** Δt where **U** is the wind vector at the steering level in the atmosphere (700 – 850 mb) and Δt is the time between successive scans. It is assumed that convective cells move in the direction which is close to the one of vector **U.** This is why knowing wind at the steering level from the model or sounding is highly recommended (although not necessary). Actual moving vector of the cells is generally different from **U** and the deviation from **U** should be estimated by displacement of the VIL peaks belonging to the same cell as described by Rosenfeld (1987) and Hu et al. (2019).

If simple advection takes place and the cell does not evolve during time shift Δt then the VIL map of this cell (or its watershed) at n+1 scan completely coincides with its VIL map at n scan after its backward shift. However, rarely happens in the nature. Usually the VIL maps of the cell are only partially overlapped and the i-th cell at n+1 scan can better overlap with the j-th cell at n scan. In order to make sure that we follow the temporal evolution of the same cell, the following logic is implemented in MCIT (Hu et al. 2019):

(1) Integral VIL is computed for each i-th cell at n scan: IntVIL(i,n)
(2) Integral VIL is computed for the overlapping area of the compared cells at scans n and n+1: IntVIL(i,j,n,n+1) if the cell (i,n) and the cell (j,n+1) are overlapped.
(3) Cell j is considered a continuation of cell i if
    (a) IntVIL(i,j,n,n+1) is more than 50% of the smaller of IntVIL(i,n) and IntVIL(j,n+1)
    (b) The VIL peaks of both old and new cells are inside the common area of the two compared cells
    (c) If the condition (c) is not fulfilled then it is required that IntVIL(i,j,n,n+1) must be more than 75% of the smaller of IntVIL(i,n) and IntVIL(j,n+1).

More details of MCIT can be found in Rosenfeld (1987) and Hu et al. (2019).

Task 8.2. Nowcasting cold season precipitation (rain and snow) using polarimetric signatures aloft

The major idea of nowcasting is to quantify snow / ice precipitation at its main source (primarily in the dendritic growth layer), calculate falling snow trajectory using the wind data, and estimate transformation of microphysical characteristics of snow along the fall trajectory using spectral bin cloud model that is initiated by the size distribution of snowflakes aloft and utilizes vertical profiles of temperature and humidity retrieved from the sounding or HRRR regional model. With DGL at the heights of 2 – 3 km above the freezing level or the ground and terminal fall velocity of snowflakes of about 1 m/s this would result in snow nowcasting with lead time of 30 – 60 min.

We illustrate this concept using an example of heavy snowfall event that occurred in the Washington, DC area on 23 January 2016. The event was closely monitored by the KLWX

WSR-88D radar located in Sterling, VA. During the storm, several snow bands passed over the DC area. The successive columnar vertical profiles (CVP, Murphy et al. 2019) of Z, Z_{DR}, ρ_{hv}, and K_{DP} were generated in the strongest snow band for a period of 2 hours as it passed from SE to NW in the proximity of the WSR-88D radar (Figs. 8.2.1 and 8.2.2). The CVPs clearly indicate that the bulk of snow manifested by very high K_{DP} (starting at 0630 UTC) is generated within the layer centered at the height of 4 km. Then falling snow starts aggregating which causes rapid increase of Z until it reaches stable and dry surface layer stretching from the ground up to 2 – 3 km (Fig. 8.2.3). Snow sublimation in the dry layer causes noticeable decrease in the snow intensity once it reaches the surface at about 0800 UTC (Fig. 8.2.2).

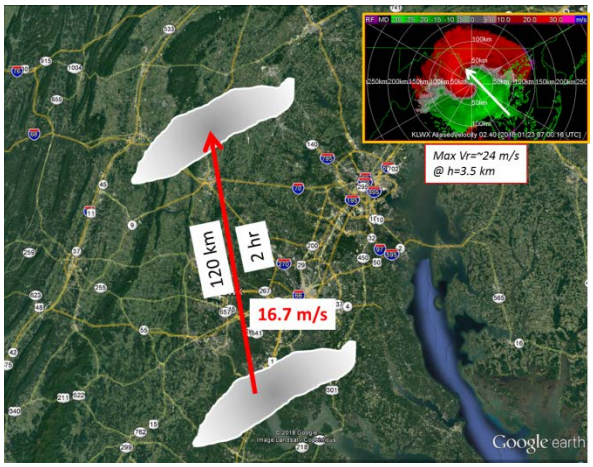

Fig. 8.2.1. Cartoon showing locations of the major snow band during heavy snowfall event in the Washington, DC area on 23 January 2016 at 0630 UTC and 0830 UTC.

Polarimetric radar-based size distribution retrieval at the 4 km level at 0630 UTC yields IWC of about 1.5 g/m^3 and mean volume diameter D_m of snowflakes of about 3.2 mm. With such initial size distribution of snow aloft, our 1D cloud model yields about 40% reduction in snow rate within dry layer with average sub-saturation with respect to ice of 5% (Fig. 8.2.3). This is well illustrated in Fig. 8.2.4 (left two panels) showing evolution of the vertical profiles of snow rate obtained from the S(K_{DP},Z) and S(Z) relations (S = 0.088Z$^{1/2}$, accepted for the US East Coast).

The polarimetric relation derived by Bukovcic et al. (2018)

$$S = 2.2K_{DP}^{0.61}Z^{0.33} \qquad (8.3)$$

yields a decrease of S from 11 – 12 mm h^{-1} aloft down to 7 - 8 mm h^{-1} near the surface. The comparison of snow rates retrieved from the radar at 0.8 km height above the Automated Surface Observation Station (ASOS) in close proximity to the radar shows that the polarimetric relation gives better estimate of maximal snow rate measured by ASOS but tends to underestimate lower

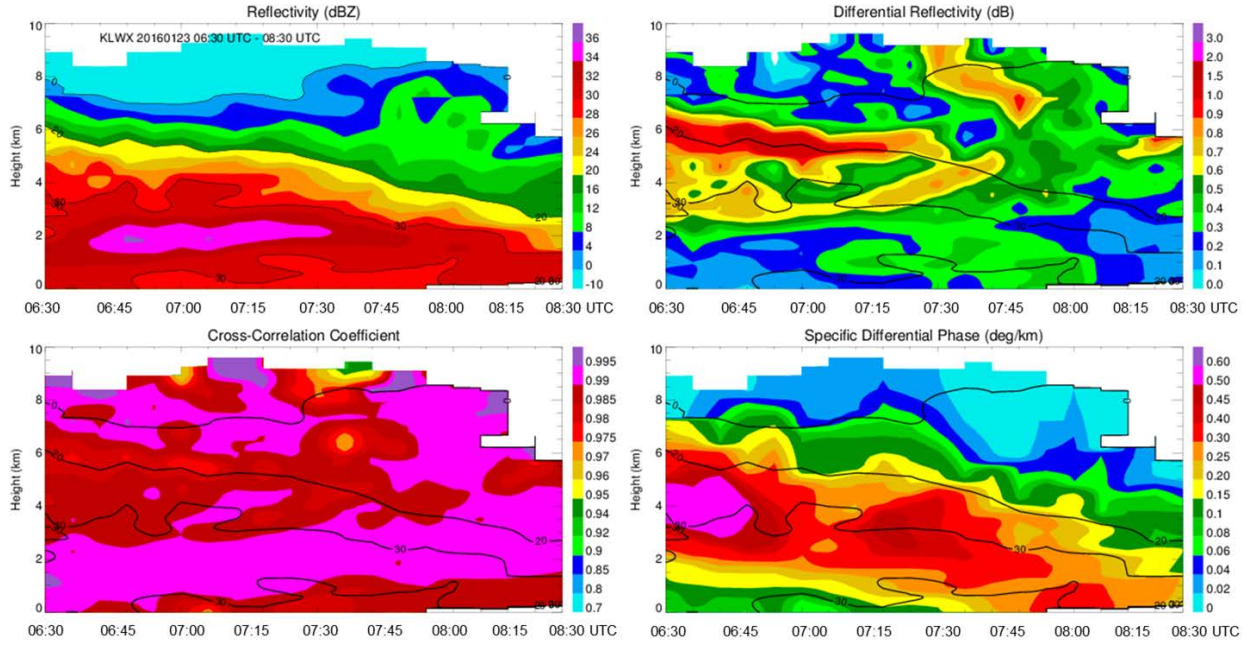

Fig. 8.2.2. Columnar vertical profiles (CVP) of radar reflectivity Z, differential reflectivity Z_{DR}, cross-correlation coefficient ρ_{hv}, and specific differential phase K_{DP} measured by the KLWX WSR-88D radar in a height versus time format as the snow band moved NW from 0630 UTC till 0830 UTC for the storm on 23 January 2016. The CVP column moves with the center of the snow band.

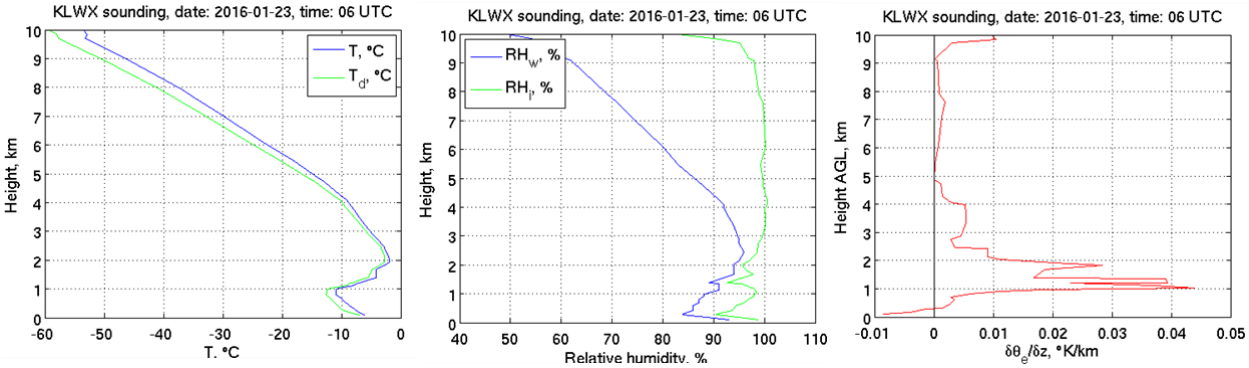

Fig. 8.2.3. Vertical profiles of temperature (T) and dewpoint temperature (T_d) (left panel), vapor saturation with respect to water and ice (RH_w and RH_i) (middle panel), and vertical gradient of potential equivalent temperature $d\theta_e/dz$ (right panel) retrieved from the sounding near the Dulles International Airport at 0600 UTC on 23 January 2016.

snow rates (right panel in Fig. 8.2.4). The S(Z) relation underestimates maximal snow rate by a factor of 2.

This example demonstrates potential capability of the method to predict snow occurrence and intensity at the surface more than 100 km away from its source aloft with lead time of 1.5 hours (in this particular example) although polarimetric relation for snow measurements may need

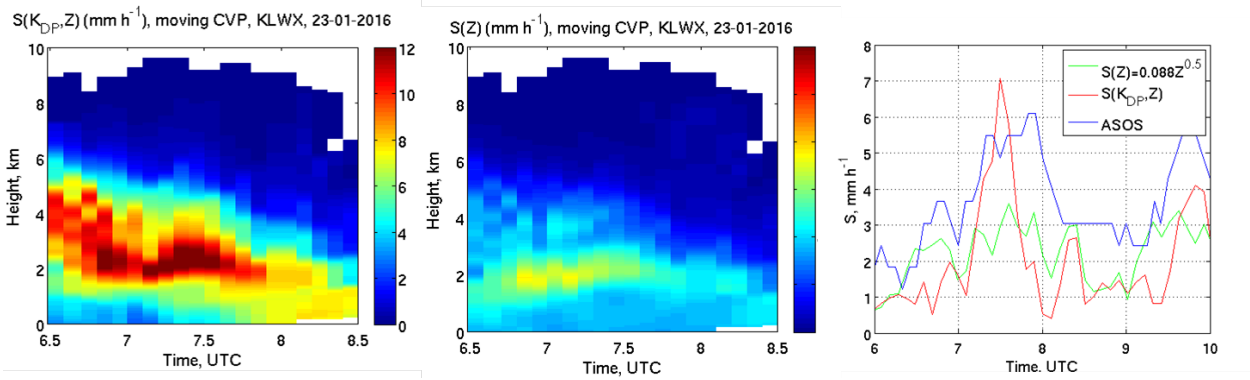

Fig. 8.2.4. Columnar vertical profiles (CVP) of snow rate retrieved from the $S(K_{DP},Z)$ and S(Z) relations (left and middle panels) columns and temporal dependencies of snow rate from the nearest ASOS (blue curve), $S(K_{DP},Z)$ (red curve), and S(Z) (green curve) (right panel).

further adjustment. Note that the described methodology may not be directly applicable for lake-effect snow events with low cloud tops well below the dendritic growth layer.

This concept of nowcasting of precipitation at the surface from the polarimatric measurements in the dendritic growth layer was tested on a large dataset in partnership with the University of Bonn, Germany (Troemel et al. 2019). Time series of quasi-vertical profiles (QVPs) from 52 stratiform precipitation events observed with the polarimetric X-band radar in Bonn/Germany (BoXPol) between 2013 and 2016 have been statistically analyzed to infer microphysical processes shaping the dendritic-growth-layer (DGL) and melting-layer (ML) signatures including surface rainfall. Specific differential phase K_{DP} in the ML shows an average correlation of 0.65 with surface rainfall for these cases. Radar reflectivity decreases below the ML by about 2 dB on average while differential reflectivity Z_{DR} is hardly affected, which suggests rain evaporation as the dominating effect. Estimated ice water content or snow water equivalent precipitation rate S in the DGL is correlated with surface rain rates with lead times of 30 min and longer, which opens a pathway for radar-based nowcasting of stratiform precipitation tendencies. Trajectories of snow generated aloft down to the surface were constructed from wind profiles derived both from the nearest radiosounding and radar-based velocity azimuth displays (VAD) to narrow down the location where the DGL-generated snow reaches the surface as rain. The lagged correlation analysis between K_{DP} in the DGL and reflectivity Z_H at that location demonstrates the superiority of the VAD information. Correlation coefficients up to 0.80 with lead times up to 120 min provide a proof of concept for future nowcasting applications that are based on DGL monitoring. Strong correlation between K_{DP} of ice in the DGL aloft and Z in rain at the surface 50 min later is illustrated in Fig. 8.2.5 (top and middle panels) for a stratiform event observed on 7 October 2014 by BoXPol. The bottom panel in Fig. 8.2.5 demonstrates very good qualitative and quantitative agreement between polarimetric estimates of snow rate in the DGL, rain rates estimated from Z at the surface, and the corresponding surface gauge measurements with a 50 min time shift.

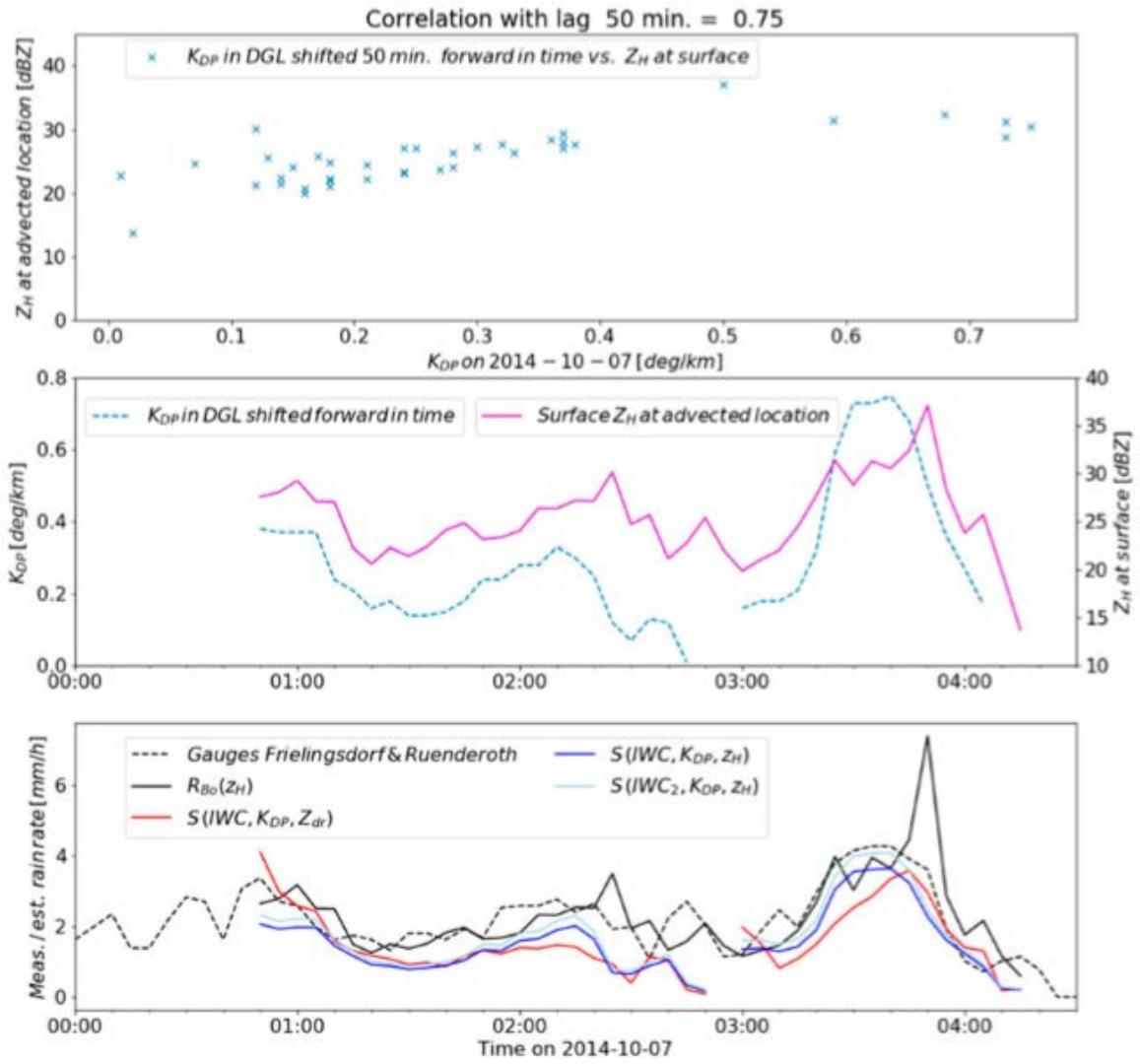

Fig. 8.2.5. (top) Scatterplot of K_{DP} in the DGL against Z at predicted surface location 50 min later, exploiting VADs, (middle) the corresponding time series of surface Z and K_{DP} in the DGL shifted forward in time, and (bottom) the R(Z)-derived and measured rain rates 50 min later at the closest rain gauges together with three S(IWC) retrievals using different polarimetric estimators, for the low-wind precipitation event observed on 7 October 2014. From Troemel et al. (2019).

8.3. Quasi-Vertical Profiles (QVP) and Column Vertical Profiles (CVP)

Novel techniques for processing and displaying polarimetric radar data such as QVP and CVP allow representing vertical profiles of radar variables and their temporal evolution with high accuracy and fine vertical resolution. The radar data are displayed in a height vs time format. A useful extension of the QVP technique – a range-defined QVP (RD-QVP) was recently introduced by Tobin and Kumjian (2017). The RD-QVP product is generated using radar data

collected at all available antenna tilts as opposed to a single elevation utilized by QVP (see Fig. 8.3.1). This improves the accuracy of radar variable estimates and fills the “surface gap” caused by

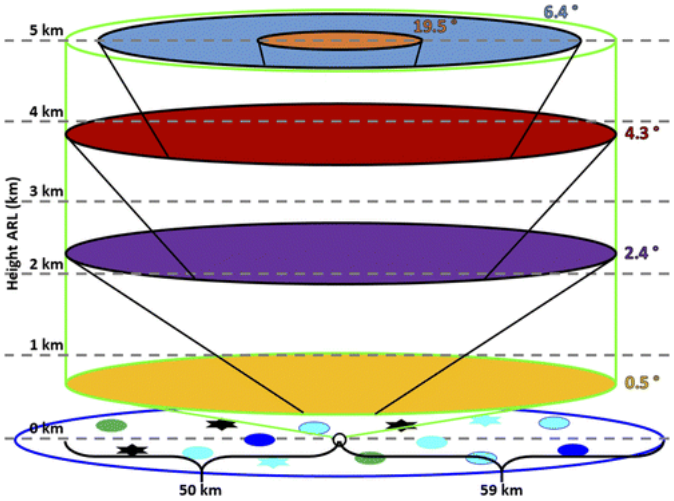

Fig. 8.3.1. Cartoon explaining the RD-QVP concept. From Tobin and Kumjian (2017).

the lack of radar data within first 8 range gates for the WSR-88D radars. Important near-surface features such as refreezing signature which are often missed in QVPs are now detectable in the RD-QVP product.

RD-QVPs and CVPs can be generated almost in real time (with about 5 min latency) for any WSR-88D radar using the Amazon Web Services (AWS) cloud computing platform. Each radar has its own rented computer that processes the data from NOAA’s Big Data project. The Amazon Web Service S_3 is used to store and display the QVP and CVP products. These data can be viewed remotely by our customers in the Radar Operations Center (ROC) and in the NWS headquarters in Washington, DC. Live RD-QVP demonstration was presented during the ROC Data Quality meeting in February 2019. At the moment, the product is in great demand by people at the Lincoln Lab and NWS. We can qualify such effort as a real breakthrough in our ability to examine and visualize WSR-88D data in real time and in the format that has not been utilized before.

Herein, we present several examples of the RD-QVP and CVP products which can be utilized by researchers and operational meteorologists. A typical composite RD-QVP is shown in Fig. 8.3.2. It represents the evolution of the vertical profiles of Z, Z_{DR}, K_{DP}, and ρ_{hv} retrieved from the data collected by the KGYX WSR-88D radar in Portland, Maine, during the Noreaster winter storm on 02/13/2019. This RD-QVP product reveals important microphysical features elucidating the process of precipitation formation aloft and its type at the surface. Three notable layers are visible in the Z_{DR} image: dendritic growth layer within a temperature interval between -10 and -20°C centered at the height of about 5 km, melting layer at 2.5 km, and refreezing layer from the altitude of approximately 1 km down to the surface. It is obvious that the melting layer associated with a temperature inversion emerges aloft starting from 06Z. It is accompanied by

the appearance of the refreezing signature beneath which tells that freezing rain in the height interval between 1 and 2 km is converting to ice at the height of 1 km. The corresponding precipitation type at the

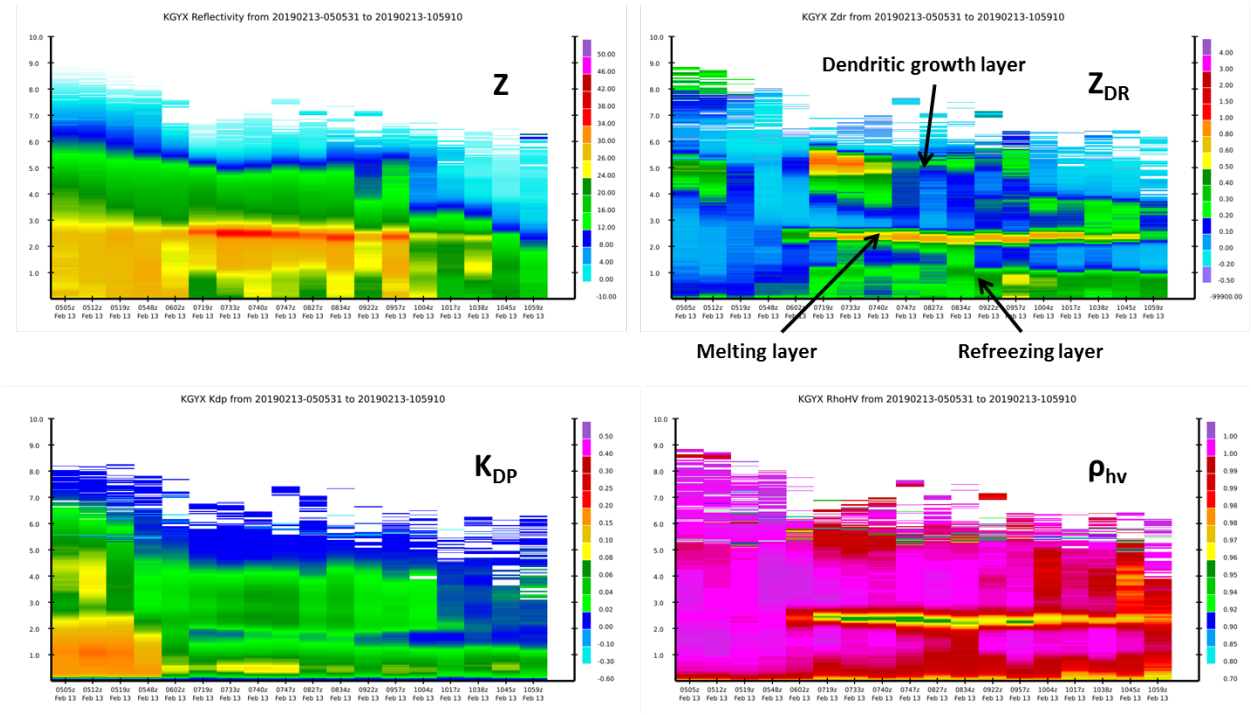

Fig. 8.3.2. RD-QVP of Z, Z_{DR},K_{DP}, and ρ_{hv} generated from the KGYX WSR-88D data during snowstorm on 02/13/2019 in the Portland, Maine area.

surface during this period is ice pellets or ice needles which were confirmed by surface observations. It is important that the elevated layer of freezing rain between 1 and 2 km poses significant icing hazard for aviation.

The sounding in the proximity of the KGYX WSR-88D radar displayed in Fig. 8.3.3 shows the presence of elevated melting layer at the time when it was detected by the radar. It also indicates that the surface atmospheric layer is sufficiently cold to activate ice nuclei in supercooled raindrops (-5 - -6°C) and to spawn the refreezing process (Reeves et al. 2016).

Another Noreaster example is illustrated in Figs. 8.3.4 and 8.3.5. The storm on 02/02/2015 was also observed with the nadir-pointing W-band airborne radar deployed onboard the NCAR Gulfstream V HIAPER aircraft. While flying over the Boston area, the W-band radar detects the melting layer at the height of about 1.5 km (Fig. 8.3.4). Notable is fine radar echo structure at the top of the storm exhibiting multiple snow generating cells which are resolved with the airborne radar. The corresponding RD-QVP product generated from the data collected by the KOKX WSR-88D radar complements the airborne radar data (Fig. 8.3.5). It also shows very clean signature of the melting layer with gradually increasing height from 1.5 to 2 km. Although the snow generating cells are not resolved in the RD-QVP product due to its poor horizontal resolution (100 km as shown in Fig. 8.3.1), the combined use of radar information retrieved from

nadir-pointing short-wavelength radar and ground-based WSR-88D radar has strong potential to better understand the physics of snow formation in winter storms.

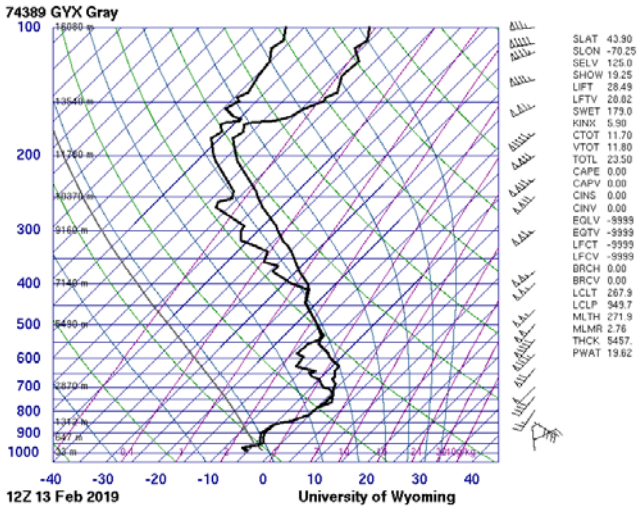

Fig. 8.3.3 Sounding in the proximity of the KGYX WSR-88D radar on 02/13/2019 at 12 Z.

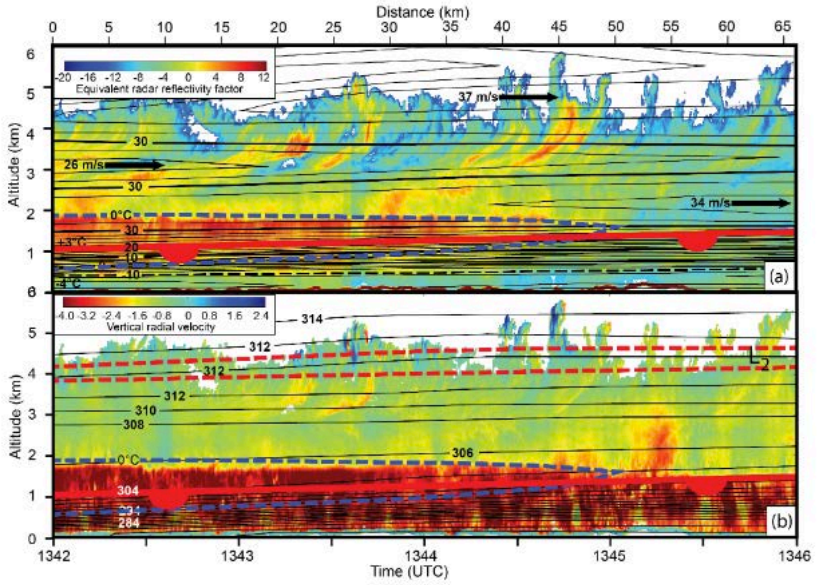

Fig. 8.3.4. Radar reflectivity (top panel) and vertical Doppler velocity (bottom panel) measured by the nadir-pointing W-band radar onboard the NCAR Gulfstream V HIAPER aircraft over Noreaster on February 2, 2015. From Janiszeski et al. (2019).

Finally, we utilized the CVP methodology to investigate the microphysical structure of land-falling hurricanes Harvey and Florence. The results of this study are summarized in the paper by Hu et al. (2019). Some excerpts from the paper are illustrated in Figs. 8.3.6 – 8.3.7.

The eyewalls of hurricanes and their outer rain bands have very different microphysical characteristics and different potentials for flash flooding. The hurricane Harvey exemplifies such

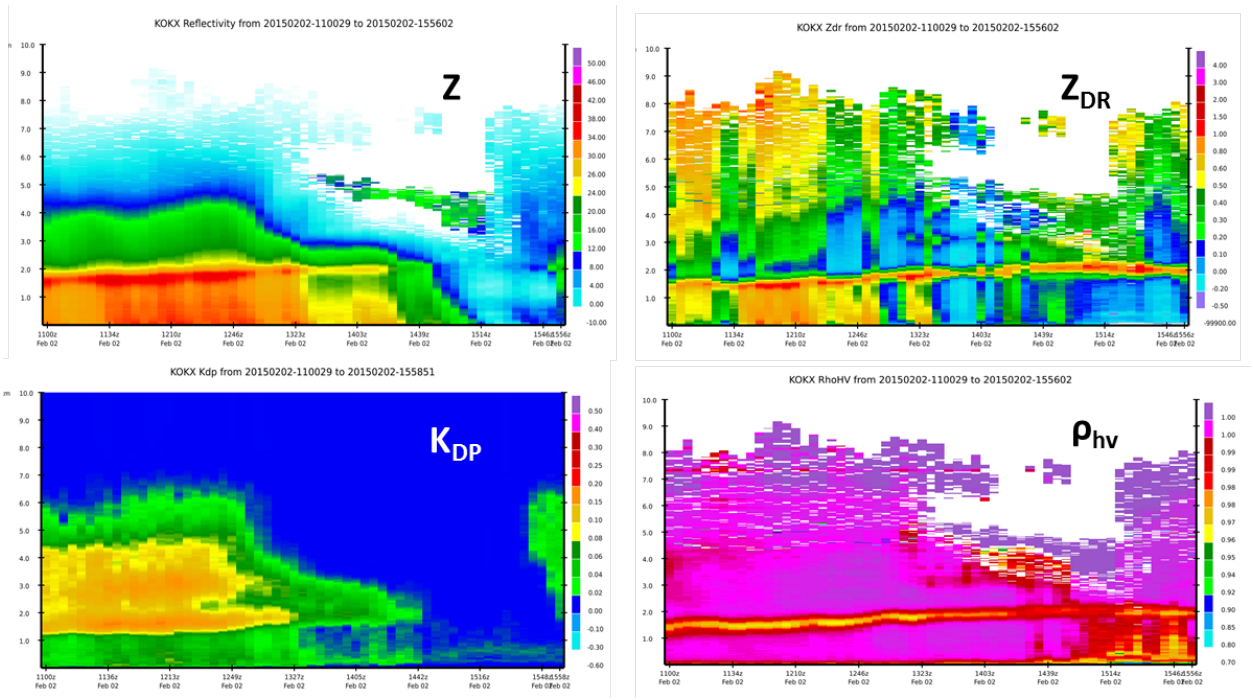

Fig. 8.3.5. Composite RD-QVP generated from the KOKX WSR-88D radar data collected on February 2, 2015 during the Noreaster event.

difference very well. The composite CVPs of polarimetric radar variables have been generated in the eyewall area of the hurricane and its outer rain bands. The centers of the vertical CVP columns are shown in the PPIs of radar reflectivity shown in Fig. 8.3.6. The eyewall region was better sampled by the KCPR WSR-88D radar in Corpus Christi (left panel in Fig.8.3.6) whereas the outer rain band was better visible from the perspective of the KHGX WSR-88D radar in Houston (right panel in Fig. 8.3.6). The corresponding CVPs are shown in Figs. 8.3.7 and 8.3.8 .In addition to the CVPs of radar variables, the CVPs of the mean ice particle diameter D_m and particle number concentration N_t were generated from the polarimetric radar data above the melting layer using the algorithms described by Ryzhkov et al. (2018) and Ryzhkov and Zrnic (2019).

Comparison of the two CVPs in the eyewall and outer rain band indicates that the eyewall region is characterized by high concentration of very small ice aloft with radar reflectivity generally below 20 dBZ above the melting layer. It is a warm rain mechanism that is primarily responsible for precipitation in the eyewall. In other words, a bulk of rain is formed below the melting layer via coalescence of raindrops and ice aloft does not play significant role in precipitation formation. The outer rain band is characterized by noticeably higher radar reflectivity in ice above the melting layer, larger size of ice particles, and lower number concentration. This means that good portion of precipitation at the surface is formed via melting of ice. Coexistence of graupel-size ice, ice crystals, and supercooled water lofted in stronger updrafts facilitates electric charge separation and significant lightning discharges in the outer rain band. No lightning was reported in the eyewall region of the hurricane Harvey.

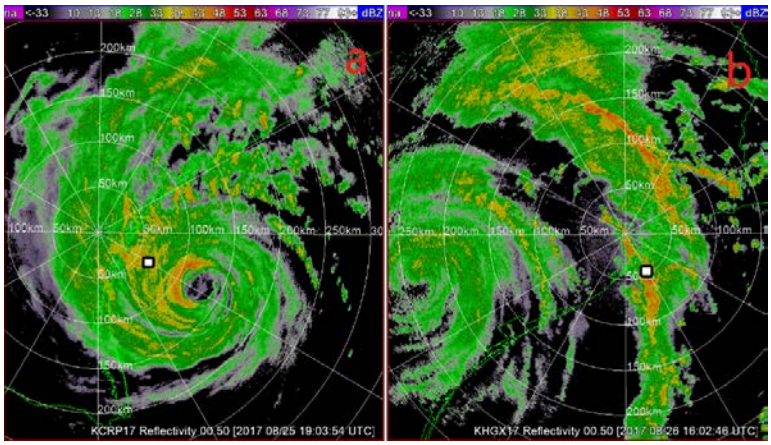

Fig. 8.3.6. Radar 0.5-degree reflectivity plan position indicator (PPI) maps. (a) Harvey's inner eyewall and (b) Harvey's outer rain band. Radar CVP sectors are labelled by the white boxes in all radar PPI panels.

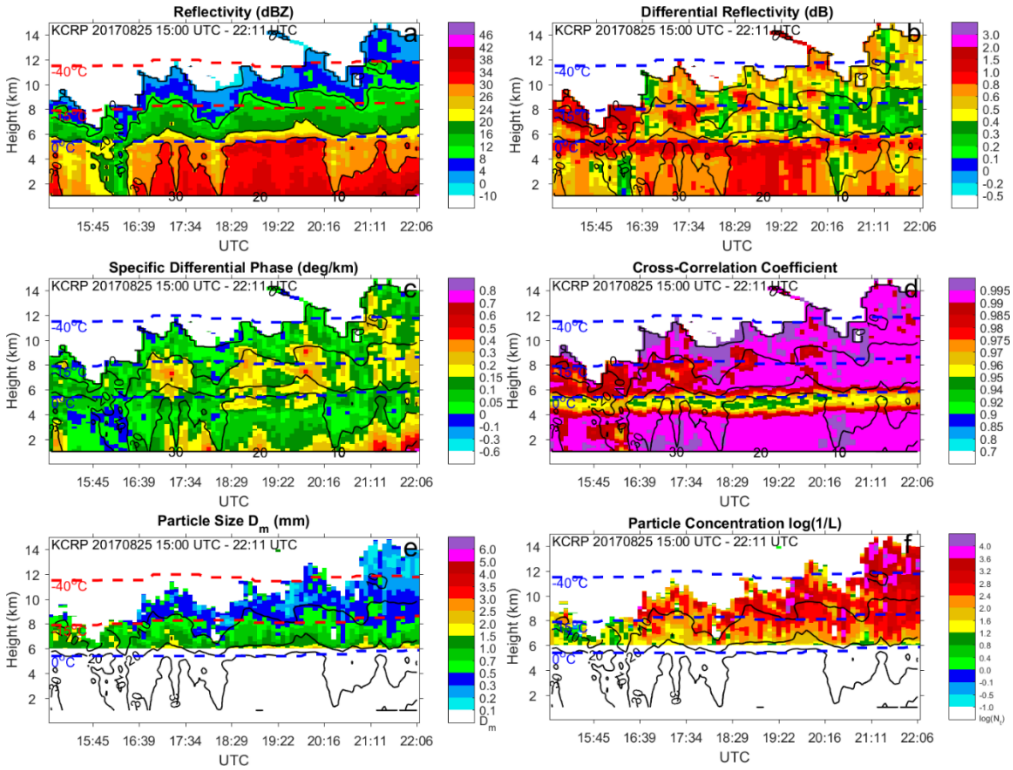

Fig. 8.3.7. CVP of Z (a), Z_{DR} (b), K_{DP} (c), ρ_{hv} (d), D_m (e) and N_t (f) of hurricane Harvey eyewall region from 20170825 15:00 UTC to 22:11 UTC. The CVP is centered at 60 km and 120° from the KCRP WSR-88D radar and the CVP base is 20 km in range and 20° in azimuth. The black contours denote reflectivity magnitudes every 10 dBZ. The dot lines in each panel show the corresponding 0° C, -15° C and -40° C isotherms from HRRR.

The combination of warm rain generated below the melting layer and rain resulting from the melting of ice originated in stronger convective updrafts makes an outer rain band of the

tropical cyclones a more efficient rain producer compared to an eyewall. Extremely heavy rain from the stalled external rain bands has caused most of the flooding during Harvey.

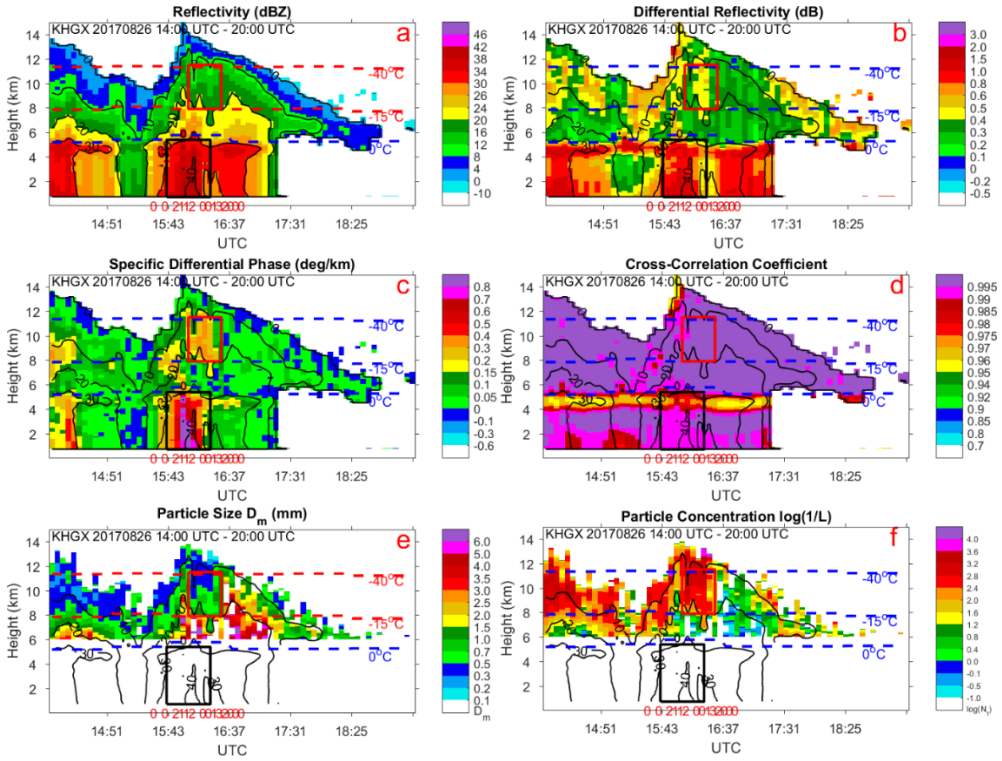

Fig. 8.3.8. Same as in Fig. 8.3.7, but for hurricane Harvey's external rain bands from 20170826 14:00 UTC to 20:00 UTC. The CVP is centered at 40 km and 150° from the KHGX radar. The red numbers at the bottom of each panel indicate the $\log_2$(#) GLM flash count within the CVP sector in each radar volume scan.

We reiterate that the advantage of CVP compared to QVP or RD-QVP is that this is not a radar-centric product and a vertical column with relatively small horizontal size where the vertical profiles of polarimetric radar variables and their temporal evolution are displayed can be placed anywhere within a radar coverage area. Moreover, such column may follow a particular storm or research aircraft. Many details of the CVP methodology can be found in the paper by Murphy et al. (2019).

Although a CVP column can be located anywhere within a radar field of view, a quality of the CVP representation inevitably degrades with the distance from the radar (as of any other radar information). Fig. 8.3.9 shows CVPs of Z created at various distances from the radar in a widespread stratiform precipitation event on February 7, 2019. This stratiform precipitation was sampled by the KCLE WSR-88D radar using VCP 215. Examination of these plots shows that, at radial distances beyond 100 km, gaps in the vertical significantly degrade the quality of the CVP.

Murphy et al. (2019) compared polarimetric radar data collected by the KVNX WSR-88D radar with in situ microphysical measurements obtained onboard of instrumented research aircraft during the MC3E field campaign in northern Oklahoma on May 20, 2011. Moving CVP was used to insure collocation of radar data with in situ aircraft measurements. The temporal

evolution of CVP moving with aircraft is illustrated in Fig. 8.3.10. Additionally, microphysical characteristics

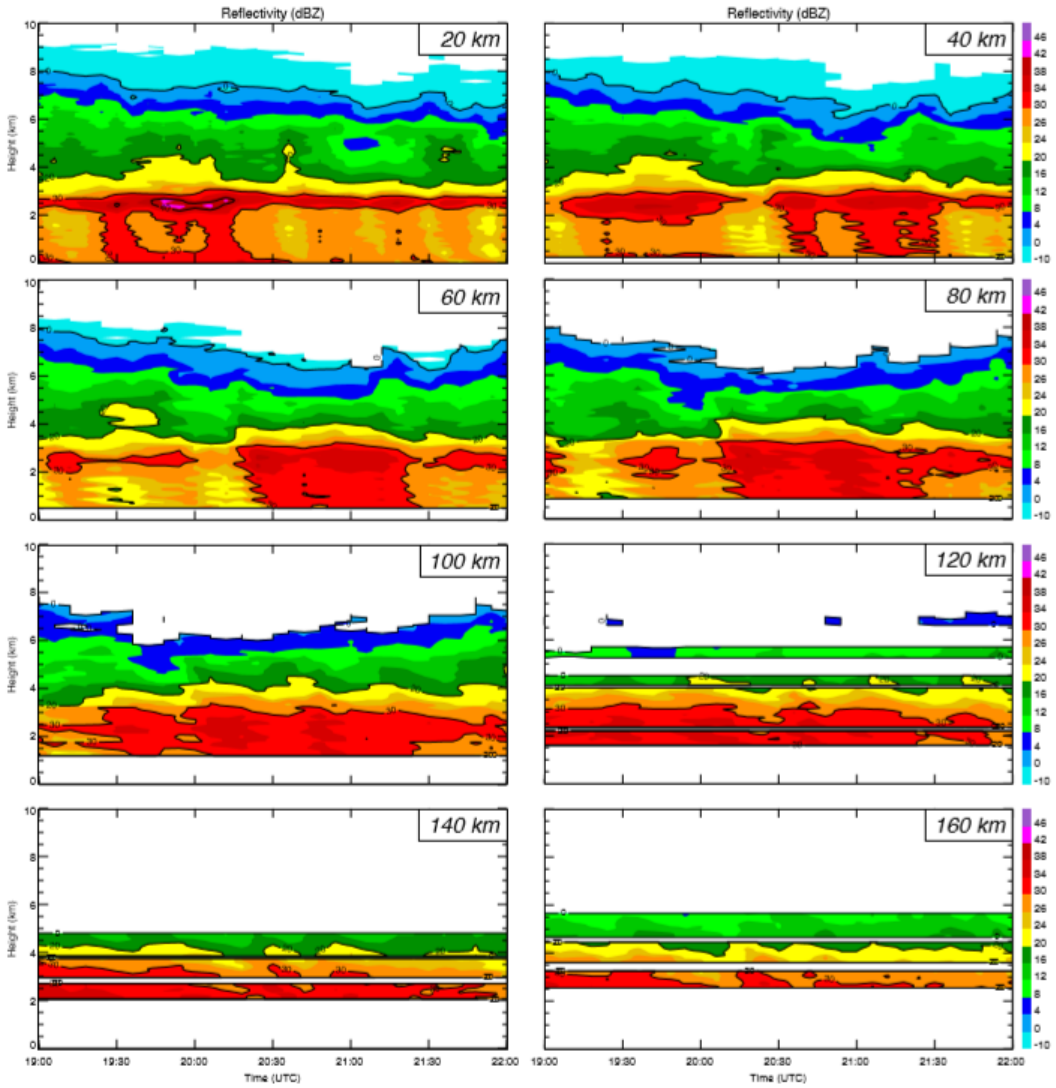

Fig. 8.3.9. CVPs of Z sampled by the KCLE WSR-88D radar on February 7, 2019. CVPs are centered at an azimuth of 225°, and at ranges from 20 km to 160 km from the radar increasing in 20 km increments. The KCLE radar was operating VCP 215 during this time period. From Murphy et al. (2019).

of ice such as ice water content (IWC), mean volume diameter of ice particles (D_m), and their total number concentration (N_t) were retrieved from the polarimetric radar measurements using the algorithm described in the monograph of Ryzhkov and Zrnic (2019) (Chapter 11). The moving CVPs of IWC, D_m, and N_t are presented in Fig. 8.3.11. The retrieved microphysical parameters of ice are in good agreement with their direct measurements onboard an aircraft (Murphy et al. 2019).

We conclude the report on Task 8.3 by providing a summary of the ROC Data Quality Team Minutes on 15 February 2019.

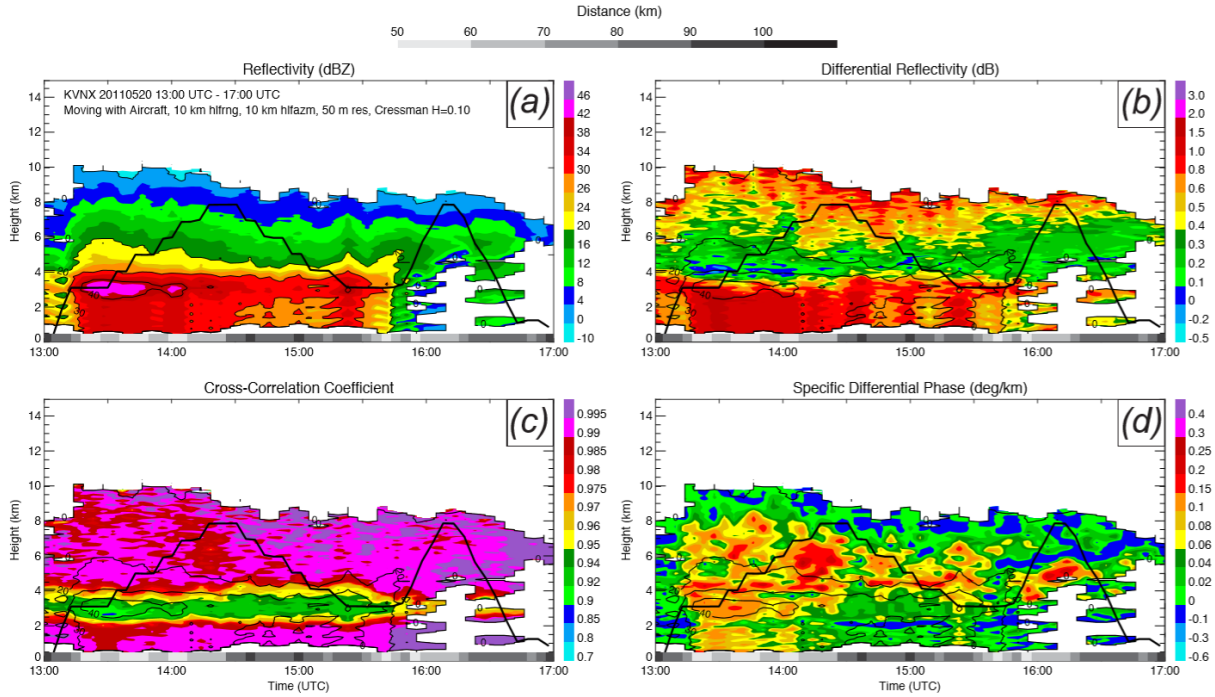

Fig. 8.3.10. Moving CVP using data from the KVNX WSR-88D radar on May 20, 2011 from 13 – 17 UTC. The CVP column moved with the location of the research aircraft flying during the MC3E campaign. The black line overlaid on each panel represents the altitude of the aircraft with time. Vertical data spacing in the CVP is 50 m, and the column base size is 20 km in range and 20° in azimuth. Distance from the radar for each scan is denoted by different shades of grey just above the x-axis on each panel. From Murphy et al. (2019).

Practical implications of QVP / CVP include:

(1) Monitoring of the height and intensity of the melting layer with high accuracy and vertical resolution.
(2) Real-time detection of the temperature inversions aloft which facilitate generation of freezing rain during cold season.
(3) Detection of the areas of strong icing hazard in the interests of aviation.
(4) Assimilation of the information about temperature and melting layer in the numerical weather prediction models.

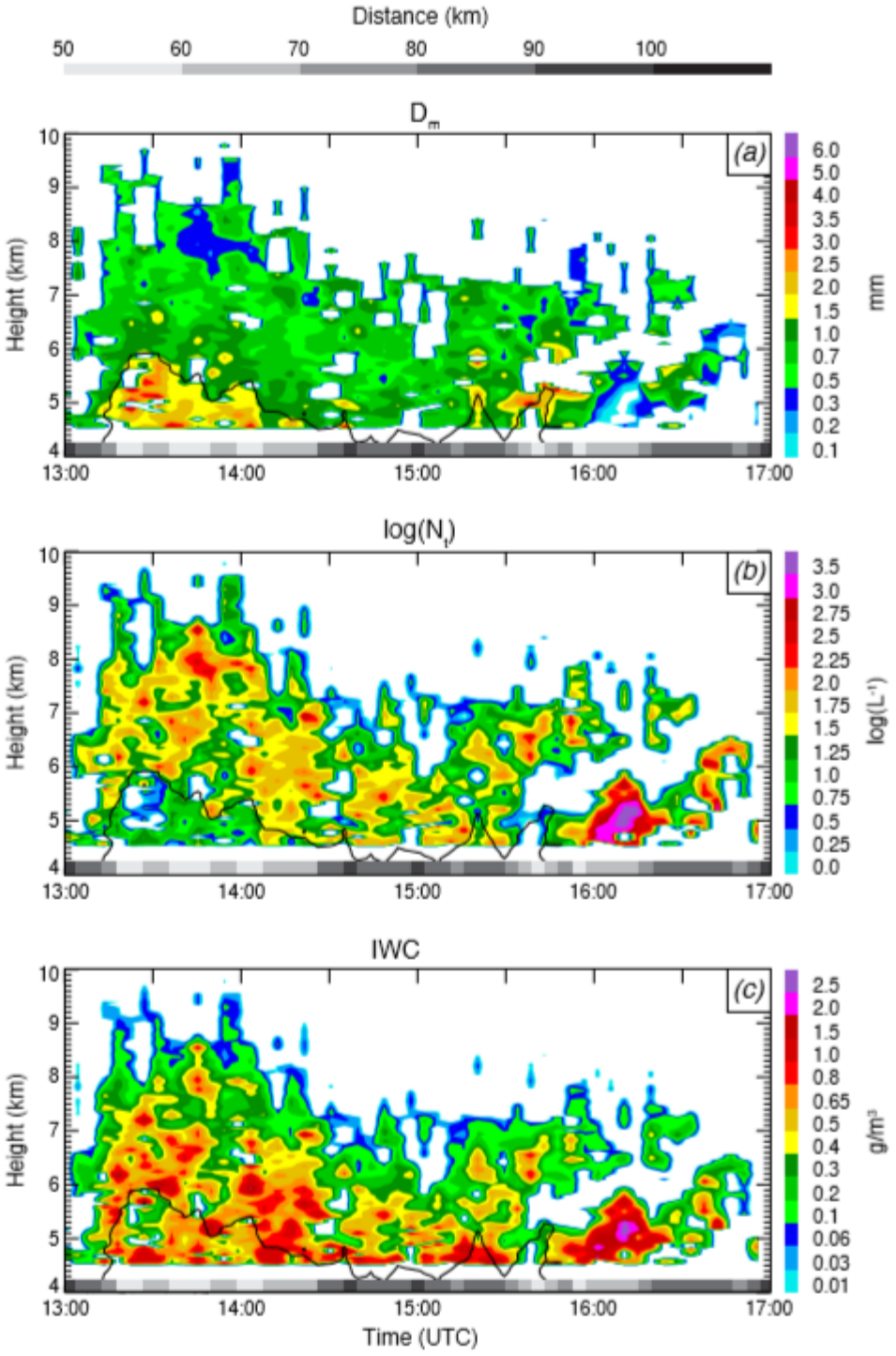

Fig. 8.3.11. Ice microphysical retrievals performed on the May 20, 2011 moving CVP. Panels are of (a) mean volume diameter D_m of ice particles in mm, (b) total number concentration N_t in log (L^{-1}), and (c) ice water content IWC in g m^{-3}. Distance from the radar for each scan is denoted by different shades of grey just above the x-axis on each panel. From Murphy et al. (2019).

Task 9.1. QPE in pure rain or rain mixed with hail.

Massive validation of the R(A) algorithm for rainfall estimation demonstrated its superior performance compared to the existing WSR-88D algorithm primarily based on the joint use of Z and Z_{DR}. A detailed description of the most recent version of the R(A) algorithm and results of its validation are summarized in the papers by Wang et al. (2019), Cocks et al. (2019), and Zhang et al. (2019). There are two lingering issues with the algorithm that have to be addressed. One of them is related to the methodology of estimating the factor α from the slope of the Z_{DR} dependence on Z and another one is the spatial variability of α within the radar coverage area.

9.1.1 Novel routine for the estimation of α from the Z_{DR} slope.

The parameter α used for the conversion of the differential span $\Delta\Phi_{DP}$ to the path-integrated attenuation PIA should be optimized on the scan-to-scan basis. At the moment, α is determined from the slope of the $Z_{DR}(Z)$ dependence which is essentially nonlinear and the value of the slope depends on the reflectivity range in which the $Z_{DR} - Z$ pairs are examined and on the maximal value of Z (or Z_m) of this range in particular. The impact of nonlinearity can be mitigated if the following formulas are utilized for computing α from the slope $K = dZ_{DR}/dZ$

$$\alpha = a_1 - a_2 K + a_3 K^2 \qquad (9.1)$$

where

$$a_1 = 0.530 - 0.0188 Z_m + 0.000194 Z_m^2 \qquad (9.2)$$

$$a_2 = 25.0 - 0.983 Z_m + 0.0103 Z_m^2 \qquad (9.3)$$

$$a_3 = 303 - 12.5 Z_m + 0.133 Z_m^2 \qquad (9.4)$$

and Z_m is the maximal Z (expressed in dBZ) in the interval (20 dBZ, Z_m) where the estimate of K is done. In other words, the polynomial coefficients in the α(K) relation depend on the maximal Z.

The performance of the new methodology is illustrated using the case of MCS on 09/16/2016 observed by the KDMX WSR-88D radar in Iowa (Fig. 9.1.1). The corresponding $Z_{DR} - Z$ dependence is shown in Fig. 9.1.2. In that case the Z_{DR} slope K is equal to 0.0556 and Z_m = 50 dBZ. The estimate of α from K using existing formula yields 0.00708 dB/deg which is less than the lower threshold 0.015 dB/deg for α. The corresponding fields of rain rate estimated with two different values of α: 0.00708 and 0.015 dB/deg are shown in Fig. 9.1.3. The comparison with gauges indicates that the use of α = 0.0708 dB/deg results in underestimation of rain rate, particularly in the squall line of MCS. Equations (9.1) – (9.4) yield the value of α equal to 0.0185 dB/deg which is more than two times larger than the previous one and is more consistent with the observed rain rate at the surface. We suggest testing this methodology on the MRMS platform in FY2020.

9.1.2. Addressing spatial nonuniformity of the factor α in the radar coverage area

The use of a single factor α for a whole radar coverage area generally leads to some underestimation of light rain and occasional overestimation of heavy rain. This is attributed to the fact that light rain is commonly characterized by larger α whereas significantly lower α might be more typical for heavier rain often associated with deep convection and the use of a single "net" α for both rain types produces such biases.

Two possible approaches are suggested to mitigate this problem. One method involves a change in the procedure to estimate path-integrated attenuation PIA from the span of total

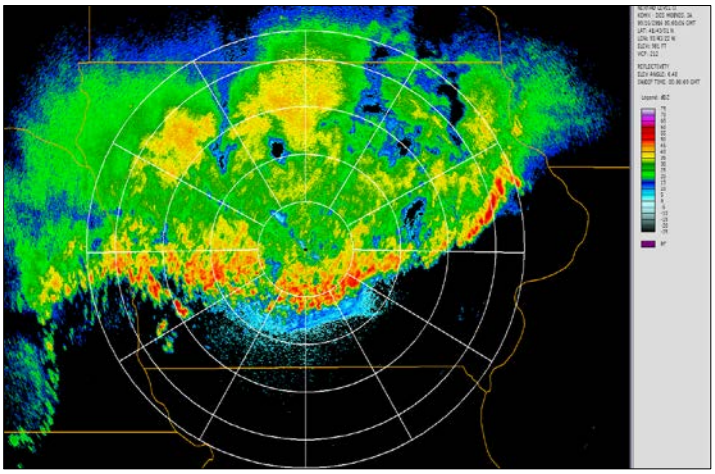

Fig. 9.1.1. PPI of Z for the MCS observed by the KDMX WSR-88D radar in Iowa on 09/16/2016.

Z	Median(Zdr)	n
20.0	0.50	3856
22.0	0.50	7154
24.0	0.53	12042
26.0	0.55	17463
28.0	0.63	22780
30.0	0.73	25380
32.0	0.84	24702
34.0	0.91	20635
36.0	0.93	14623
38.0	1.00	10808
40.0	1.13	9807
42.0	1.31	8720
44.0	1.54	7186
46.0	1.76	5722
48.0	2.00	3855
50.0	2.25	2089

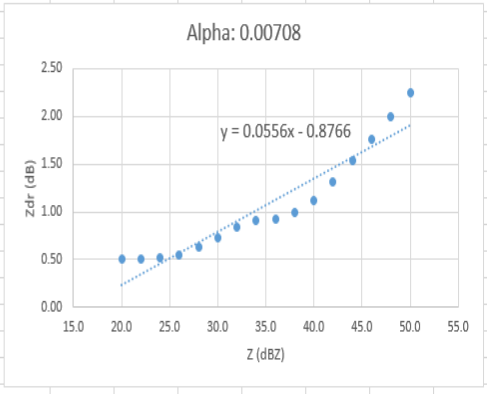

Fig. 9.1.2. Z_{DR} – Z dependence for the MCS case on 09/16/2016 with the Z_{DR} slope K equal to 0.0556.

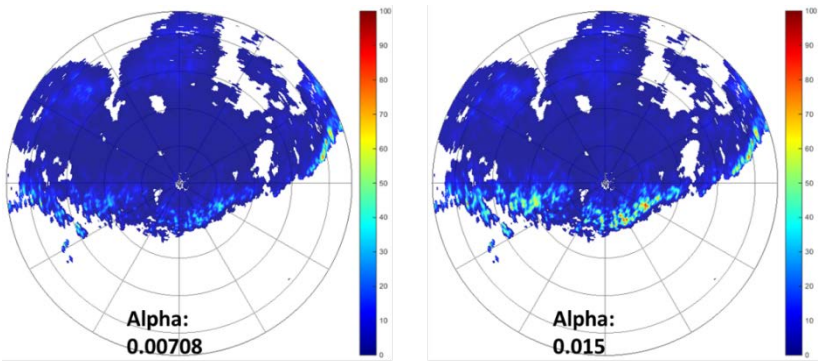

Fig. 9.1.3. Maps of rain rates obtained for two different values of α for the case of MCS on 09/16/2016.

differential phase $\Delta\Phi_{DP}$ along the radial. According to the existing version of the R(A) algorithm described in Wang et al. (2019),

$$PIA = \alpha \, \Delta\Phi_{DP} \qquad (9.5)$$

where α is determined from the Z_{DR} slope. Two-way path-integrated attenuation PIA is equal to the integral of specific attenuation A along the propagation path in rain:

$$PIA = 2\int A(s)ds \qquad (9.6)$$

This equation can be rewritten as

$$PIA = 2\int \alpha(s) K_{DP}(s) ds = 2\int \alpha(s)\, p(s) [Z(s)]^d ds \qquad (9.7)$$

where $\alpha(s) = A(s)/K_{DP}(s)$ and assuming that

$$K_{DP}(s) = p(s)[Z(s)]^d \qquad (9.8)$$

Integrating both sides of Eq (8.8) over the propagation path in rain gives

$$\Delta\Phi_{DP} = 2\int p(s)[Z(s)]^d ds \qquad (9.9)$$

Assuming p(s) constant along the ray (p(s) = p), we can arrive at the estimate of the factor p (which can vary from ray to ray)

$$p = \frac{\Delta\Phi_{DP}}{2\int [Z(s)]^d ds} \qquad (9.10)$$

and Eq (9.7) can be written as

$$PIA = \Delta\Phi_{DP} \frac{\int \alpha(s)[Z(s)]^d \, ds}{\int [Z(s)]^d \, ds} \qquad (9.11)$$

In other words, the ratio of two integrals in the right side of Eq (9.11) is used instead of a single value of α (as in (9.5)). If α is not a function of range s, then Eqs (9.11) and (9.5) become equivalent. Note that possible biases of Z due to radar miscalibration or partial beam blockage are cancelled out in the ratio in (9.11) and the estimate of PIA is immune to such biases of Z.

Since parameter α strongly depends on differential reflectivity Z_{DR} as shown in Fig. 9.4 (left panel), the range dependence of α is a well defined function of Z_{DR} which can be approximated by

$$\alpha = 0.008 + \frac{0.009}{Z_{DR} - 0.03} \qquad (9.12)$$

if $Z_{DR} > 0.2 - 0.3$ dB.

Such methodology does not require estimation of the net α from the Z_{DR} slope and automatically takes into account variability of α along the ray and in a whole radar coverage area. However, it is prone to the calibration errors of Z_{DR} measurements which are still not appropriately addressed on the WSR-88D network.

Another possible approach implies estimation of the net value of α (α_0) from the Z_{DR} slope K using new α(K) relations (9.1) – (9.4). Three next steps follow.

(1) Estimation of specific attenuation A from the basic ZPHI formula as specified in Wang et al. (2019)

(2) Conversion of A to Z(A) using equation

$$Z(dBZ) = 79.8 + 15.4 \log(A) \qquad (9.13)$$

(3) Estimation of rain rate as

$$R = 4120 A^{1.03} \frac{f[Z(A)]}{\alpha_0} \qquad (9.14)$$

where

$$f[Z(A)] = 0.0125 + 3.42\,10^{-4} x + 3.42\,10^{-5} x^2 + 1.73\,10^{-6} x^3 \qquad (9.15)$$

and $x = 50 - Z(A)$.

The underlying idea is to take into account the dependence of the factor α on radar reflectivity Z illustrated in the right panel in Fig. 9.1.4. Since Z can be biased due to radar miscalibration, partial beam blockage, or wet radome, it is recommended to use Z retrieved from A as prescribed by Eq (9.13) because specific attenuation is not biased by these factors. The function f[Z(A)] approximates a median α(Z) dependence indicated by a solid line overlaid on the scatterplot in

the right panel of Fig. 9.1.4. The numerator in the ratio in (9.14) describes the dependence of α on Z and the denominator takes into account general rain type (e.g., tropical vs continental).

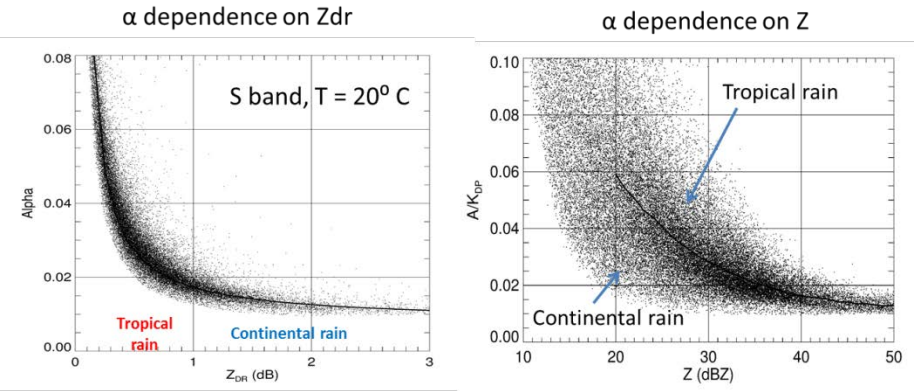

Fig. 9.1.4. Scatterplots of the factor α vs Z_{DR} and Z at S band and temperature 20°C obtained from disdrometer measurements in Oklahoma.

9.2. QPE in snow and mixed precipitation

9.2.1 Validation of polarimetric algorithms for snow quantification using surface snow measurements

Enormous variability in snow size distributions (SSDs), density, orientation, shape, crystal habits, water content, etc., introduces large uncertainty in snow measurements. Historically, a multitude of S(Z) power-law relations have been used for snow estimation but the spread of the S(Z) estimates is roughly an order of magnitude. The advent of polarization opens new possibilities to quantify snow habits and reduce the uncertainty in radar measurements. In the study of Bukovcic et al. (2018), bivariate power law relations for snowfall rate (S) utilizing specific differential phase K_{DP} and horizontal reflectivity factor Z have been derived using 2D video disdrometer (2DVD) measured snow size distributions (SSDs). These disdrometer-based relations have been validated via theoretical simulations/derivations and tested using actual polarimetric radar measurements in a number of snowstorms. As a result of studies performed in FY2019, a generalized $S(K_{DP}, Z)$ relation is developed and a novel concept of polarimetric snow measurements using a combination of K_{DP} and Z_{dp} (reflectivity difference in linear units, $Z_{dp} = Z_h - Z_v$) is introduced.

The disdrometer-based relations $S(K_{DP}, Z) = \gamma K_{DP}^{\alpha} Z^{\beta}$ (Bukovčić et al. 2018) obtained from the Oklahoma snow measurements are validated utilizing theoretical approach with exponential and gamma SSDs used in computations. We assume the SSD shape factor μ varying from -1 to 3 (which should encompass most frequently occurring snow SSDs), aspect ratio of snowflakes 0.65, and the width of the canting angle distribution σ = 0°, to be consistent with the previous study. The dependencies of snow density and terminal velocity of the snowflakes on their equivolume diameter from Brandes et al. (2007) are taken into account in the computations

of polarimetric variables at S band using the Rayleigh approximation. A theoretical $S(K_{DP},Z)$ relation for a factor $\mu = 0.135$ of a gamma shape SSD gives the relation

$$S\left(K_{DP},Z\right)=1.48K_{DP}^{0.6}Z^{0.33}, \tag{9.16}$$

which is almost identical to the one obtained from the 2DVD SSD measurements:

$$S\left(K_{DP},Z\right)=1.48K_{DP}^{0.61}Z^{0.33}. \tag{9.17}$$

A multiplier in a theoretical $S(K_{DP},Z)$ power-law relation varies from 1.93 to 0.88 for μ between -1 and 3, with the value of 1.52 for $\mu = 0$ while the exponent is almost invariant.

An analytical approach for $S(K_{DP}, Z)$ derivation is presented next. If we start from the general definition of snowfall rate S

$$S=0.6\times10^{-3}\pi\int_{0}^{D\max}\frac{\rho_s\left(D\right)}{\rho_w}D^3V_s\left(D\right)N\left(D\right)dD, \tag{9.18}$$

after the integration and series of derivations we obtain the following expression (using $\sigma = 0°$ and $b/a = 0.65$ to be consistent with Bukovčić et al. 2018):

$$S\left(K_{DP},Z\right)=1.68K_{DP}^{0.64}Z^{0.36}, \tag{9.19}$$

which is very close to the relation (9.17) derived from the Oklahoma 2DVD dataset. Both exercises confirm the validity of the previous approach.

A generalized $S(K_{DP}, Z)$ relation obtained from the Oklahoma 2DVD dataset and valid for the entire range of σ (0° – 40°) and b/a (0.5 – 0.8) for aggregated snow (and possibly across different geographical regions) is

$$S(K_{DP},Z)=\frac{2.79\times10^2}{\left(F_oF_s\right)^{0.61}}\left(\frac{p_0}{p}\right)^{0.5}(K_{DP}\lambda)^{0.61}Z^{0.33}. \tag{9.20}$$

The orientation factor $F_o = (1/2)\exp(-2\sigma^2)[1+\exp(-2\sigma^2)]$ is a function of the width of the canting angle distribution σ (in radians). The shape factor $F_s = L_b - L_a$ is a function of an aspect ratio b/a and determined by the shape parameters L_a and L_b (see Eq. (18) in Bukovčić et al. 2018). In (9.20), λ is the radar wavelength expressed in mm.

The ratio $(p_0/p)^{0.5}$ (where p and p_0 are the atmospheric pressures at the measurement level and at the surface) represents particle's terminal velocity correction due to the air density change with the altitude

Additionally, a novel $S(K_{DP}, Z_{DR})$ polarimetric relation is suggested. It has a form

$$S(K_{DP}, Z_{DR}) = 1.09 \times 10^{-2} \left(\frac{p_0}{p} \right)^{1/2} \frac{K_{DP}\lambda}{1 - Z_{dr}^{-1}} D_m^{0.15} \qquad (9.21)$$

where

$$D_m = 2 \left(\frac{Z_{dp}}{K_{DP}\lambda} \right)^{1/2} \qquad (9.22)$$

is the mean volume diameter of snowflakes. In (9.21) – (9.22), $Z_{dr} = 10^{0.1 Z_{DR}(dB)}$ and $Z_{dp} = Z_h - Z_v$.

As opposed to the S(K_{DP}, Z) relation, the S(K_{DP}, Z_{DR}) estimate is almost invariant to the variations of the particles' aspect ratio and the width of the canting angle distribution but is sensitive to some extent to the change in the particle's density (riming). It is also prone to the measurement errors of Z_{DR} including those caused by its miscalibration. Both polarimetric relations do not work well for very low values of K_{DP} and Z_{DR} which are quite typical for heavily aggregated dry snow near the surface. Therefore, it might be necessary to project the estimates of snow rate made aloft (where K_{DP} and Z_{DR} are usually higher) to the surface which may invoke cloud modeling considerations.

The performance of the S(K_{DP},Z) and S(K_{DP},Z_{DR}) relation has been evaluated for number of snowstorms. Herein, we present three examples. One of them is the 23 January 2016 East Coast blizzard which produced almost 50 mm of snow water equivalent (SWE) accumulation (Fig. 9.2.1. Instantaneous snowfall rates from the (K_{DP}, Z), S(K_{DP}, Z_{dp}), and S(Z) estimates and the reference gauge are presented in Fig. 9.2.1a whereas their accumulations are in Fig. 9.2.1b. The radar estimates are obtained at the 1.45° Plan Position Indicator (PPI) elevation, which is about 2.3 km above the ground level (~74 km east-northeast from the Sterling, Virginia WSR-88D radar). The radar snowfall rate estimates and accumulations are obtained from the rectangular area (~10 by 10 km, ~320 data points) averages, centered above the ground ASOS station (BWI) used for verification. The times of the measurements aloft are adjusted for the average terminal velocity of snowflakes, ~ 1 m s^{-1}, to match the gauge measurements (about 35 minutes offset).

During the periods of light snow, from 0000 to 0400 UTC and 1400 to 1800 UTC, S(Z) estimate is slightly better than the ones from S(K_{DP}, Z) and S(K_{DP}, Z_{dp}), and it is opposite within the moderate to high (>2.5 mm h^{-1}) snowfall rates (Fig. 9.2.1a). The S(K_{DP}, Z) relation (with $\sigma \approx 11°$ and b/a = 0.6) reproduces the snowfall rate peaks (4.5-5.5 mm h^{-1}) very well, almost matching the gauge measurements (4.5-5 mm^{-1}). But in few other periods (e.g. 0630 UTC), it overestimates S up to 2 mm h^{-1}. The S(K_{DP}, Z_{dp}) peaks are slightly smaller but comparable with the gauge's. In contrast, the S(Z) estimate does not show the peaks of SWE over 3.1 mm h^{-1} during the entire storm.

The accumulations from S(K_{DP}, Z) (red line, Fig. 9.2.1b) are very close to the gauge measurements (~46.5 mm, red line). The S(K_{DP}, Z_{dp}) estimate is not far behind (~42 mm, green line), but S(Z) is significantly smaller (~29.5 mm). The estimates from 0.5° radar elevation (not

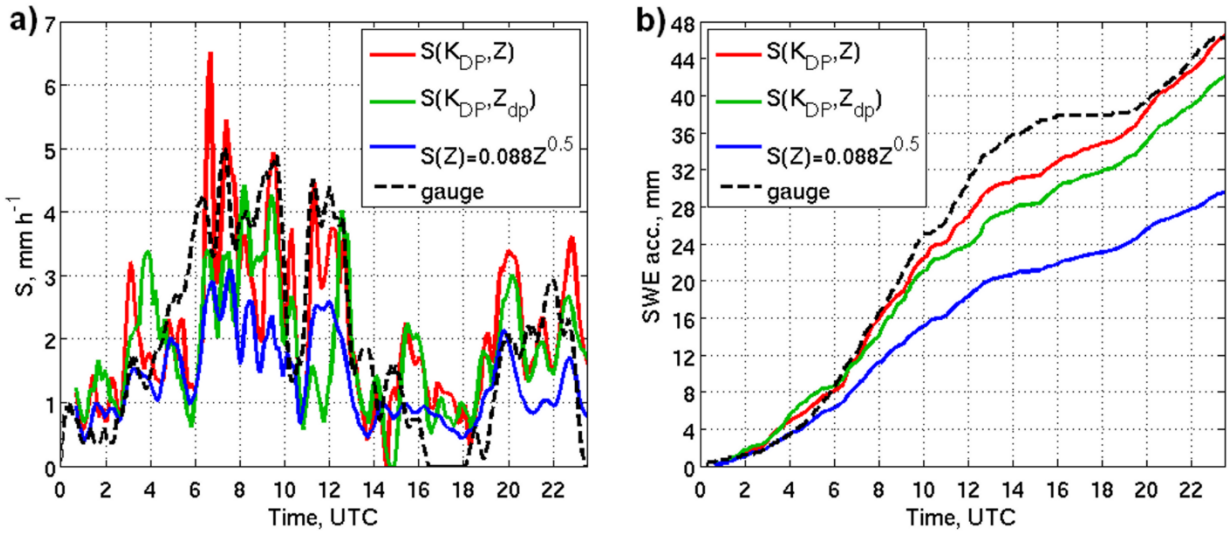

Fig. 9.2.1 (a) Snowfall rate (mm h^{-1}) estimates from ASOS gauge (dashed line), S(K_{DP}, Z) (red line), S(K_{DP}, Z_{DR}) (green line), and S(Z) (blue line), and (b) their respective accumulations; KLWX WSR-88D radar, VA, 23 January 2016.

shown, ~1.04 km AGL) display similar tendencies; S(K_{DP}, Z) peaks somewhat higher (7.8 mm at 0630 UTC, $\sigma \approx 18.5°$) but the estimate is close to the ground reference (48 mm vs. 46.5 mm). In contrast, total accumulation from S(K_{DP}, Z_{dp}) estimate is somewhat lower (~38.5 mm) whereas S(Z) is bit higher (~32.5 mm) with respect to their 1.45° counterparts. This is expected because the impact of aggregation on S(Z) is strongest at the lowest elevations. In opposite, S(K_{DP}, Z_{dp}) works the best at the temperature range from -10°C to -20°C within the dendritic growth layer. Temperatures (obtained from Rapid Refresh – RAP model, not shown) varied from -8°C to -2°C at the level of radar measurements, with the warmest period from 0300 to 1100 UTC (-2°C to -4°C) which not optimal for S(K_{DP}, Z_{dp}) estimates.

Figs. 9.2.2 and 9.2.3 illustrate the performance of a traditional and polarimetric algorithms for snow QPE for the February 1, 2011 winter storm in central Oklahoma and for the January 28, 2013 case in Grand Mesa, Colorado. In all three cases, the polarimetric method shows improvement, particularly at the times of high snowfall rate. It is important to emphasize that the polarimetric relations provide more realistic vertical profiles of snow rates than the S(Z) relation as Fig. 9.2.4 shows where a vertical structure of Z, K_{DP}, Z_{DR}, and snow rate S is displayed for the Oklahoma snowstorm. Indeed, bulk of snow is generated within the dendritic growth layer (DGL) within a temperature interval between -10 and -20°C. Snow aggregation below DGL does not change the snow flux which is reflected in the vertical profiles of S retrieved from polarimetric measurements whereas rapid decrease of S(Z) with height below DGL is apparently false.

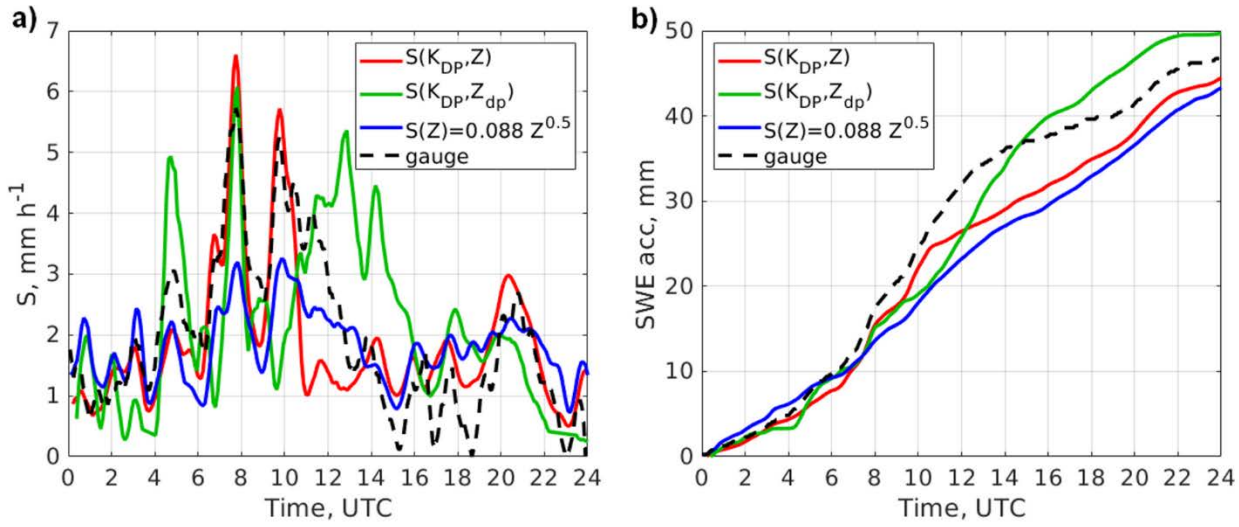

Fig. 9.2.2. Same as in Fig. 9.2.1 but for the snow case in Oklahoma

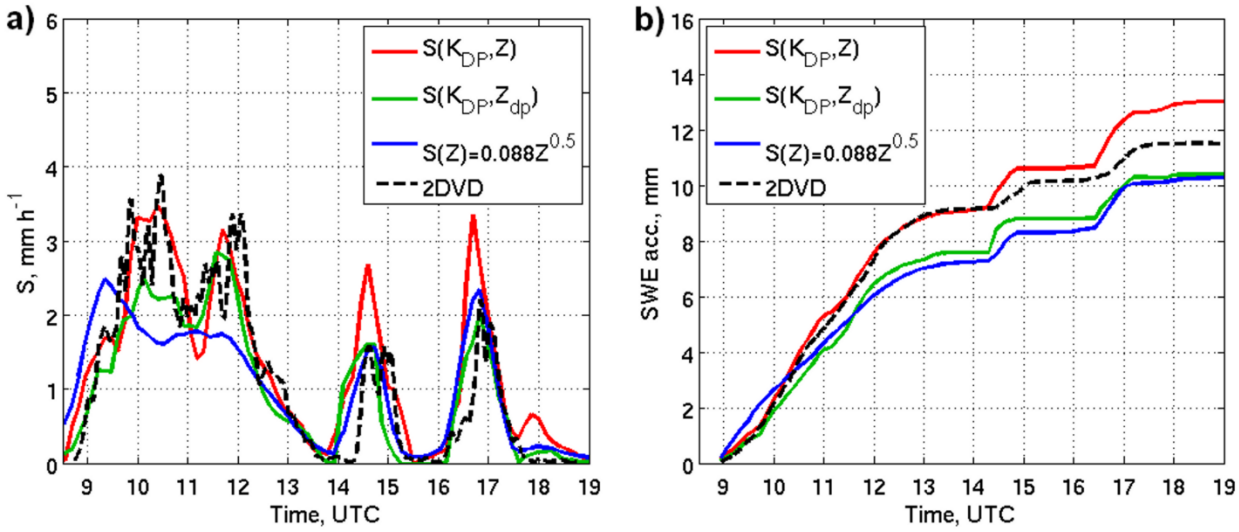

Fig. 9.2.3. Same as in Fig. 9.2.1 but for the snow case in Colorado.

9.2.2. Polarimetric Vertical Profile of Reflectivity (PVPR) technique

Bright band (BB) contamination and radar beam overshooting of rain at longer distances from the radar cause large biases in rainfall estimation over large areas of radar coverage. Existing correction methods called “vertical profiles of reflectivity” (VPR) are based on the climatology of vertical profiles of Z in stratiform rain and are not very efficient. The use of polarimetry may offer possible improvement because the areas of BB contamination are very well delineated in the fields of polarimetric variables such as Z_{DR} and ρ_{hv}. An example of PPIs of Z and ρ_{hv} at elevations 0.5 and 1.45° measured by the KICT WSR-88D radar during a low-bright-band stratiform rain event on December 19, 2011 is shown in Fig. 9.2.5. The areas of BB contaminations are very well depicted by the reduction of ρ_{hv} at both antenna tilts. Note that

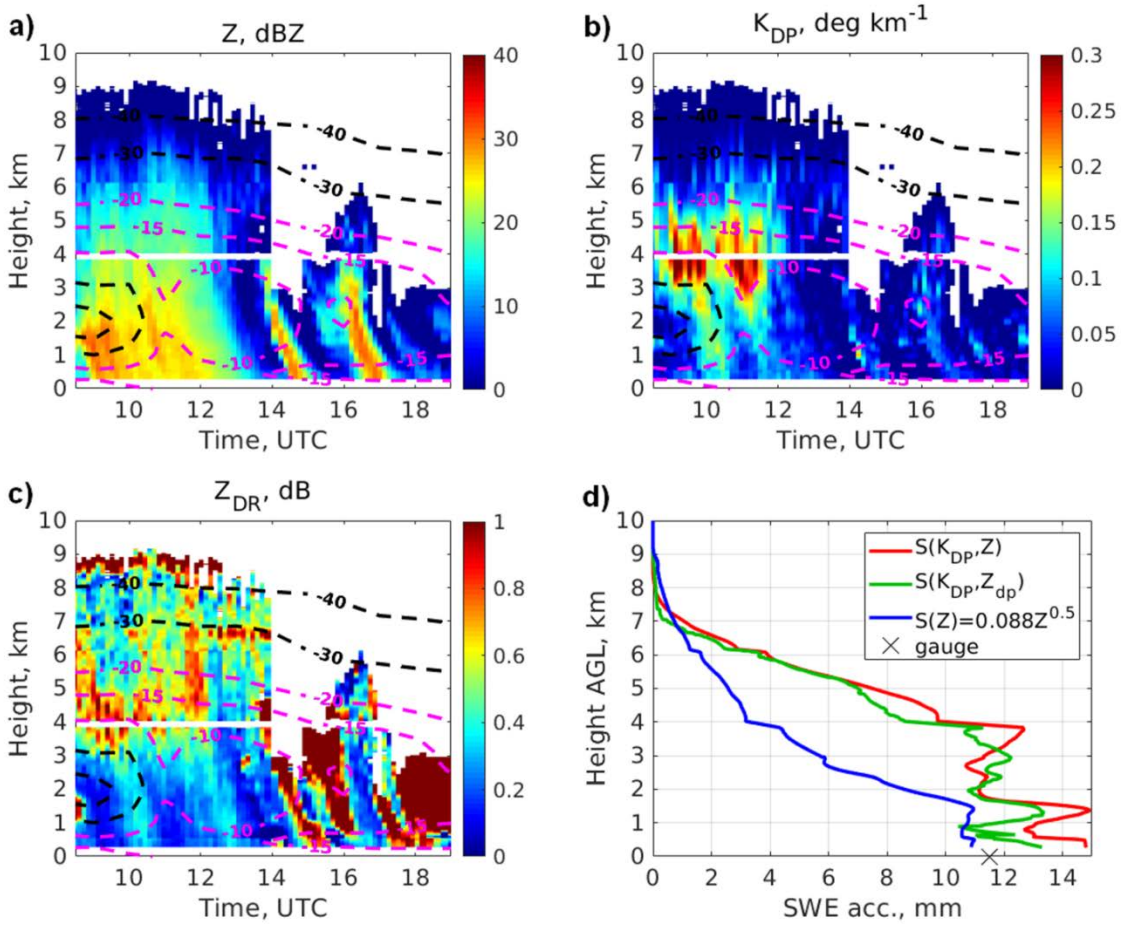

Fig. 9.2.4. QVPs of Z, K_{DP}, and Z_{DR} (panels a, b, and c) and vertical profiles of snow accumulations estimated from the S(Z), S(K_{DP},Z), and S(K_{DP},Z_{DR}) relations for the snowstorm in Oklahoma on February 1, 2011.

some enhancement of Z is produced by embedded convection in this case and its contribution has to be separated from the artificial enhancement caused by the bright band contamination.

The suggested methodology called "polarimetric VPR" or PVPR is based on the correlation of the vertical profiles of Z and ρ_{hv} within the melting layer which is best quantified using "quasi-vertical profiles" (QVP) technique. Establishing statistical correlations between intrinsic vertical profiles of Z and ρ_{hv} through the melting layer using QVP methodology is a starting point of PVPR. Then a multitude of model intrinsic vertical profiles of Z and ρ_{hv} in the ML is created and a pair of radial profiles of Z bias and ρ_{hv} is generated and stored in lookup tables for every pair of intrinsic profiles by taking into account beam broadening. An example of intrinsic (or "true") vertical model profiles of Z and ρ_{hv} is presented in Fig. 9.2.6 and the corresponding radial model profiles by BB-related bias of Z (ΔZ) and ρ_{hv} are shown in Fig. 9.2.7 for two pairs of the intrinsic vertical profiles of Z and ρ_{hv}. One of the pairs corresponds to stronger ML with higher ΔZ and lower ρ_{hv} in Fig. 9.2.7 (curves marked by 1) whereas another pair produces lower ΔZ and shallower ρ_{hv} signature in the model radial profile of ρ_{hv} (marked by 2). Because the

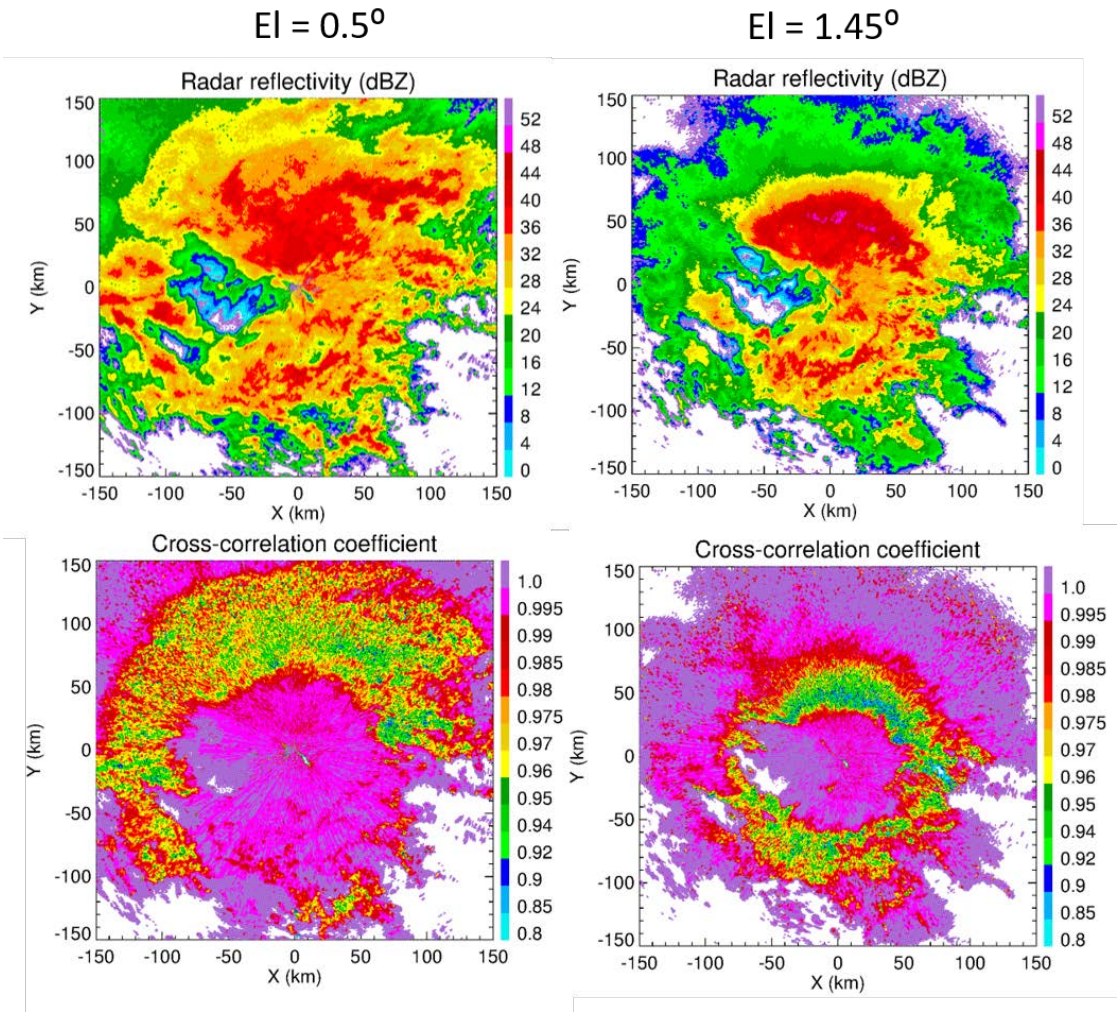

Fig. 9.2.5. PPIs of Z and ρ_{hv} at elevations 0.5° and 1.45° measured by the KICT WSR-88D radar on December 19, 2011.

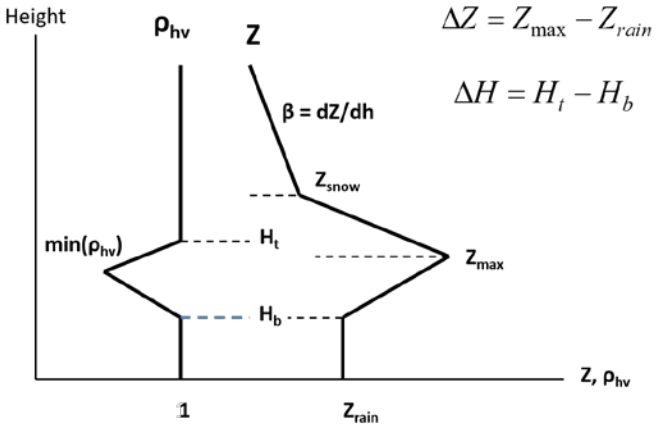

$$\Delta Z = Z_{\max} - Z_{rain}$$

$$\Delta H = H_t - H_b$$

Fig. 9.2.6. Example of intrinsic vertical model profiles of Z and ρ_{hv} through the ML.

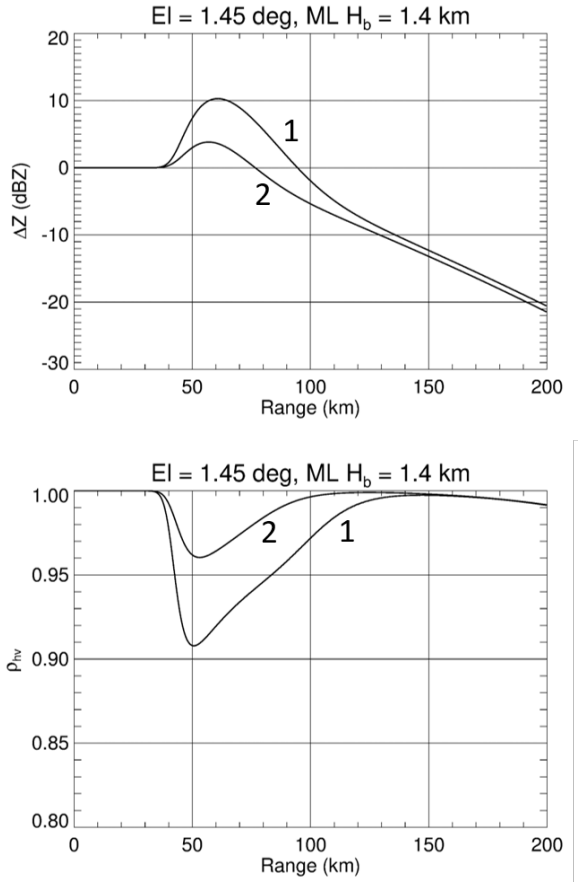

Fig. 9.2.7 Simulated radial profiles of Z bias and ρ_{hv} at El = 1.45° for the ML with its bottom at the height of 1.4 km for two different values of intrinsic minimal ρ_{hv} within the ML (as depicted in Fig. 9.2.6).

vertical and radial profiles of Z (or ΔZ) are correlated, one can predict stronger enhancement of Z within BB for lower ρ_{hv}. In other words, it is possible to quantify the BB-related Z bias using radial profile of ρ_{hv}. The whole idea of PVPR is to examine a measured radial profile of ρ_{hv} at a given elevation and find its best match in the family of model radial profiles stored in the lookup tables. The corresponding radial profile of ΔZ has to be subtracted from the measured radial profile of Z.

In order to match the model and measured radial profiles of ρ_{hv}, two parameters are estimated (1) the distance where ρ_{hv} starts dropping due to BB contamination and (2) the "strength" of the ML which is an integral parameter defined by Eq (7.1) that can be reliably estimated even from the noisy ρ_{hv} (see Fig. 7.2.4). From the first one, a height of the "true" bottom of the ML (not affected by beam broadening) is determined. Azimuthal profiles of the distances to the ML bottom along the beam at elevation 1.45° and the corresponding height of the bottom of the ML are displayed in Fig. 7.2.6.

The result of the PVPR correction of Z at elevation 1.45° is presented in the left bottom panel of Fig. 9.2.8. The biases of Z related to BB contamination are substantially reduced. This is also confirmed by the consistency of the corrected Z field at the elevation 1.45° (left bottom panel) and observed Z field at elevation 0.5° in area of BB contamination at higher tilt (right bottom panel). The result of the correction of a radial profile of Z at El = 1.45° is shown in Fig. 9.2.9. Uncorrected profile of Z exhibits an artificial bump which is eliminated by PVPR and the corrected profile of Z at higher elevation becomes very similar to the one at lower elevation.

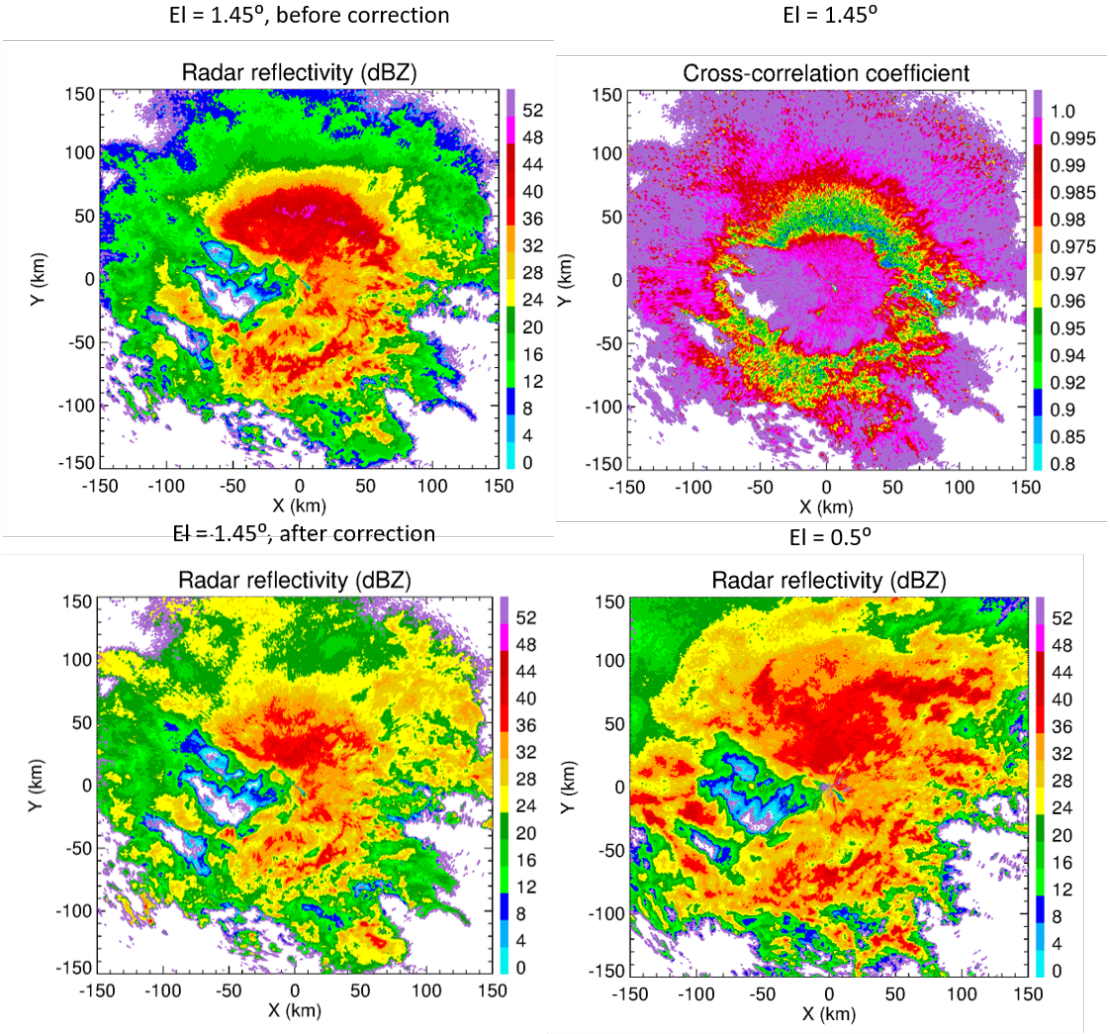

Fig. 9.2.8. PPIs of (left top panel) Z at El = 1.45º before correction, (right top panel) ρ_{hv} at El =1.45º, (left bottom panel) Z at El = 1.45º after correction, and (right bottom panel) Z at El = 0.5º for the case on December 19, 2011.

Another challenging case of low bright band is taken from the Western US where the beam blockage at lower elevations is ubiquitous (see Fig. 9.2.10). The radar beams at elevations 0.5°and 0.9° are obviously blocked in wide sectors whereas higher tilt at elevation 1.3° is not blocked but is more affected by the BB contamination. Again, we were able to retrieve azimuthal

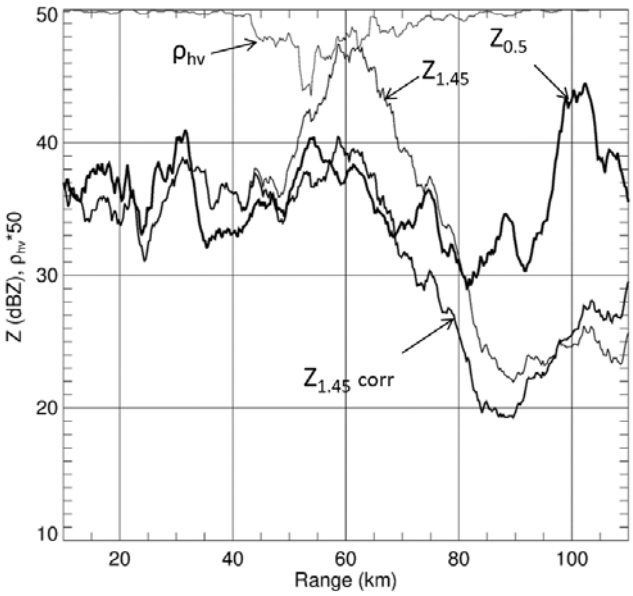

Fig. 9.2.9. Radial profiles of Z at El = 1.45º before and after PVPR correction, Z at El = 0.5º, and ρ_{hv} at El = 1.45º.

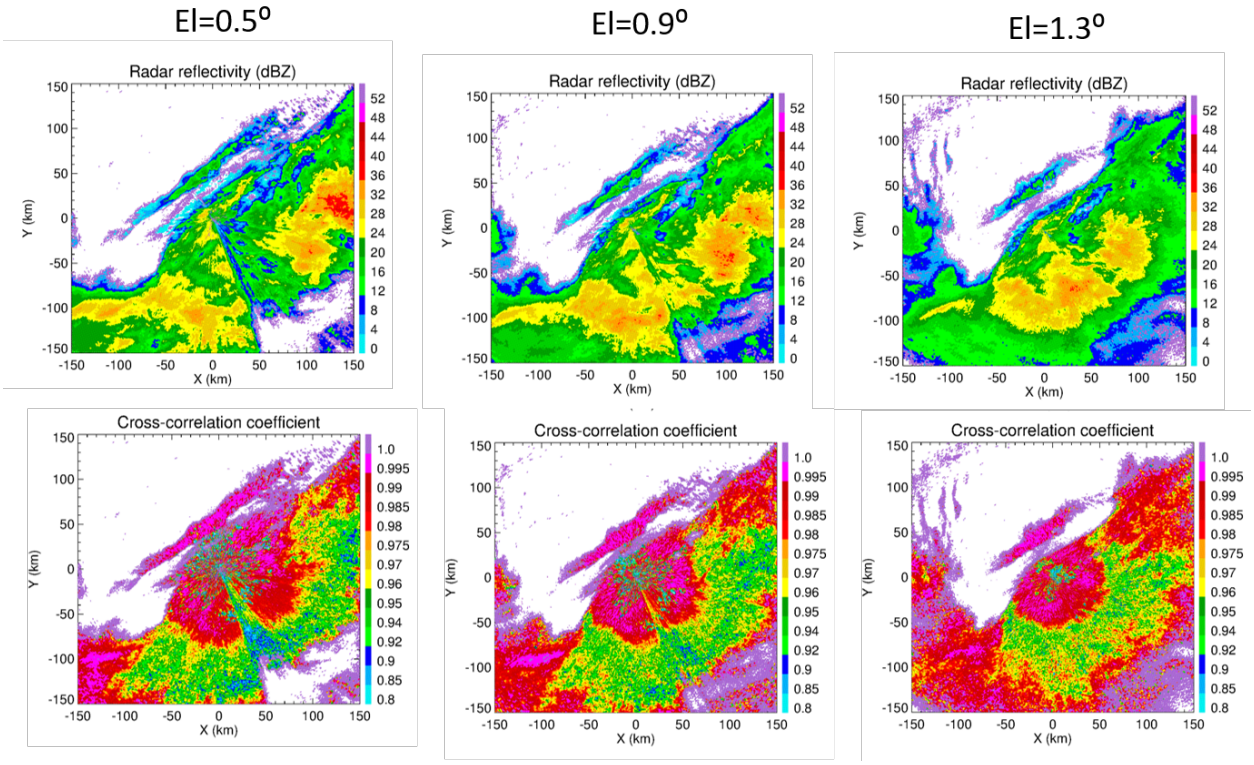

Fig. 9.2.10. PPIs of Z and ρ_{hv} at antenna elevations 0.5, 0.9, and 1.3º obtained from the measurements by the KRLX WSR-88D radar on February 18, 2019.

profiles of the ML height and strength using the PVPR methodology (Fig. 9.2.11) and eliminate BB contamination at elevation 1.3° (Fig. 9.2.12). Indeed, no arc-shaped artificial enhancement of Z is visible anymore (right bottom panel of Fig. 9.2.12).

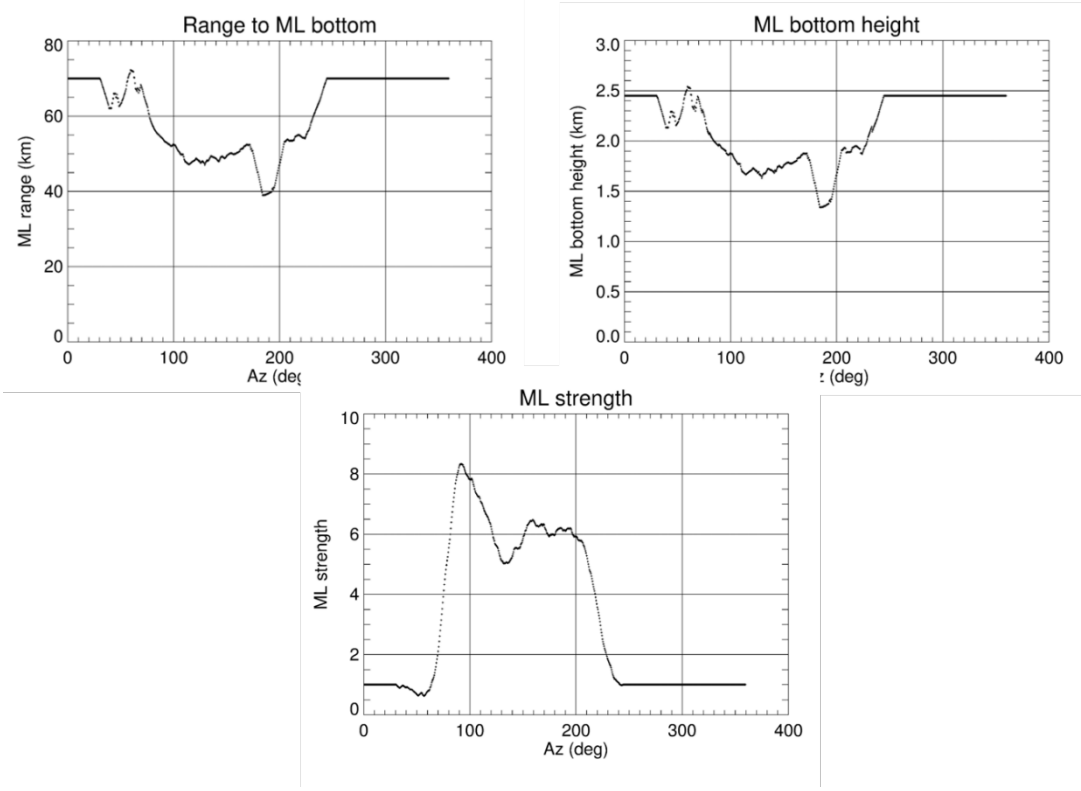

9.2.11. Azimuthal dependencies of the radial distance to the ML bottom, ML bottom height, and "strength" of the ML retrieved from the data collected at El = 1.3º for the case on February 18, 2019.

In summary, the following conclusions can be drawn regarding PVPR

(1) The suggested PVPR technique shows good promise in two challenging situations: (a) BB enhancement of Z is mixed with the increase of Z due to embedded convection and (b) Z at lower tilts is biased by partial beam blockage.
(2) The current version of PVPR takes into account azimuthal and range heterogeneity of the rain field and melting layer.
(3) As a byproduct, the PVPR technique allows to estimate "true" heights of the bottom and top of the melting layer which are not affected by beam broadening although radial resolution of such designation degrades with the distance from the radar.
(4) The PVPR methodology makes a good use of higher antenna elevations for QAPE I situations when the data at lowest elevation are of poor quality due to ground clutter contamination or beam blockage.

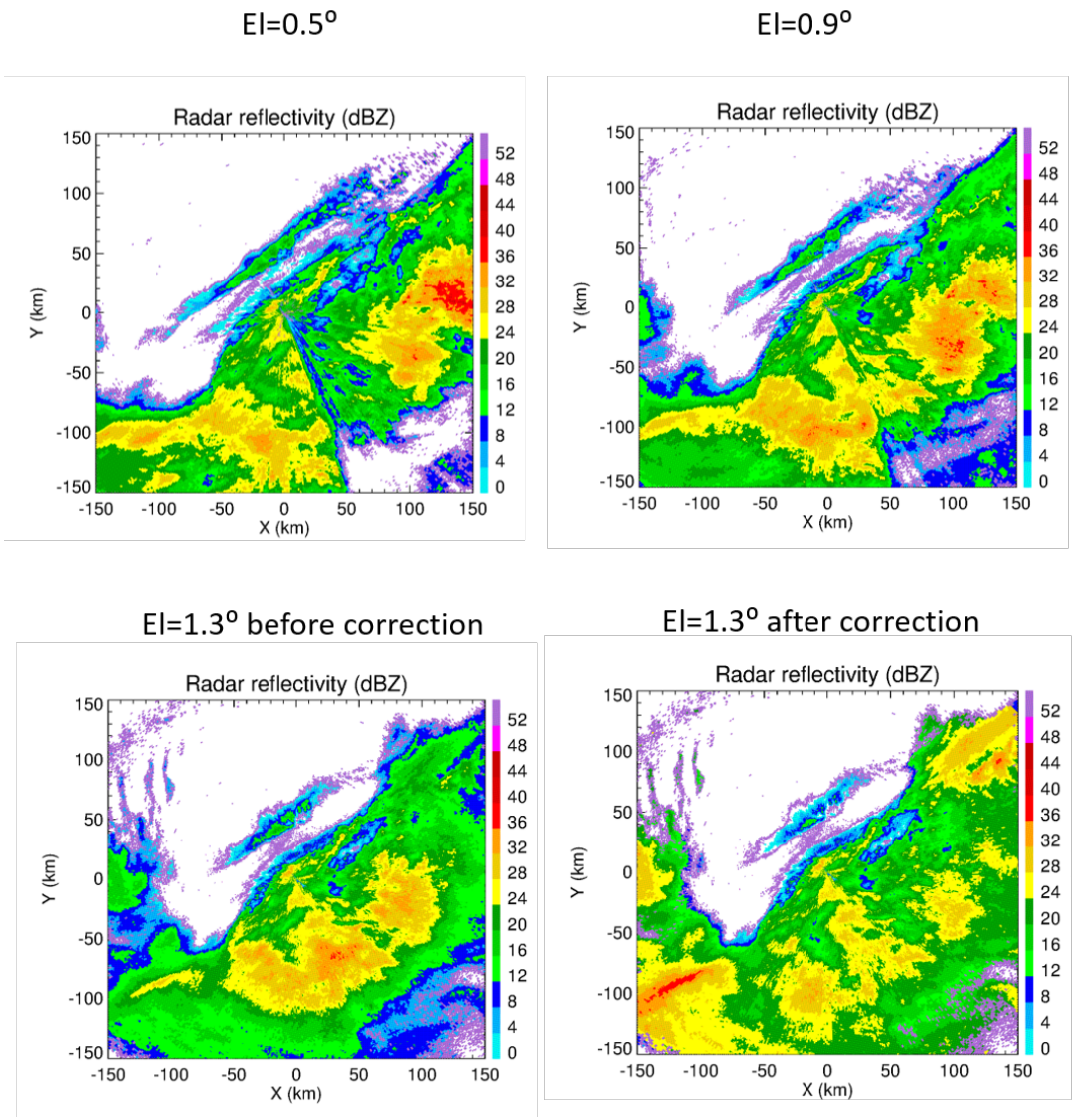

Fig. 9.2.12. PPI of Z at El = 0.5 and 0.9º (top panels) and Z at El = 1.3º before and after PVPR correction (bottom panels) for the case on February 18, 2019.

Publications during FY2019

Monograph

Ryzhkov, A., and D. Zrnic, 2019: *Radar Polarimetry for Weather Observations*. Springer Atmospheric Sciences, 486 pp.

Journal articles

Bukovcic, P., A. Ryzhkov, and D. Zrnic, 2019: Polarimetric relations for snow estimation – radar verification. *J. Appl. Meteor. Clim*., submitted.

Carlin, J. and A. Ryzhkov, 2019: Estimation of melting layer cooling rate from dual-polarization radar: Spectral bin model simulations. *J. Appl. Meteor. Clim.*, **58**, 1485 – 1508.

Cocks, S., Y. Wang, L. Tang, A. Ryzhkov, P. Zhang, J. Zhang, and K. Howard, 2019: A prototype quantitative precipitation estimation algorithm for operational S-band polarimetric radar utilizing specific attenuation and specific differential phase: Part II – Case study analysis and performance verification. *J. Hydrometeorology*, **20**, 999 – 1014.

Griffin, E., T. Schuur, and A. Ryzhkov, 2019: A polarimetric radar analysis of ice microphysical properties in melting layers of winter storms using S-band quasi-vertical profiles. *J. Appl. Meteor. Clim.*, conditionally accepted.

Hu, J., D. Rosenfeld, D. Zrnic, E. Williams, P. Zhang, J. Snyder, R. Orville, A. Ryzhkov, E. Hashimshoni, R. Zhang, R. Weitz, 2019: Multiple Convective Cell Identification and Tracking Algorithm for documenting time-height evolution of polarimetric radar variables and lightning properties. *Atmospheric Research*, **226,** 192 – 207.

Hu, J., D. Rosenfeld, A. Ryzhkov, and P. Zhang, 2019: Synergetic use of the WSR-88D radars, GOES-R satellites, and lightning sensors to study microphysical characteristics of hurricanes. *J. Appl. Meteor. Clim*., submitted.

Kuster, C. M., J. C. Snyder, T. J. Schuur, T. T. Lindley, P. L. Heinselman, J. C. Furtado, J. W. Brogden, and R. Toomey, 2019: Rapid-update radar observations of Z_{DR} column depth and its use in the warning decision process. *Wea. Forecasting*, **34**, 1173-1188.

Murphy, A., A. Ryzhkov, and P. Zhang, 2019: Columnar Vertical Profiles (CVP) methodology for validating polarimetric radar retrievals in ice using in situ aircraft measurements. *J. Atmos. Oceanic Tech.,* to be submitted.

Troemel, S., A. Ryzhkov, B. Hickman, K. Muhlbauer, and C. Simmer, 2019: Polarimetric radar variables in the layers of melting and dendritic growth at X band – implications for a nowcasting strategy in stratiform rain. *J. Appl. Meteor. Clim*., **58,** 2497 – 2522.

Wang, Y., S. Cocks, L. Tang, A. Ryzhkov, P. Zhang, J. Zhang, and K. Howard, 2019: A prototype quantitative precipitation estimation algorithm for operational S-band polarimetric radar utilizing specific attenuation and specific differential phase: Part I – Algorithm description and initial results. *J. Hydrometeorology*, **20**, 985 – 997.

Zhang, J., L. Tang, S. Cocks, P. Zhang, A. Ryzhkov, K. Howard, C. Langston, and B. Kaney, 2019: A dual-polarization radar synthetic QPE for operations. *J. Hydrometeorology*, submitted.

Conference papers

Bang, W., J. Carlin, A. Ryzhkov, K. Kim, G. Lee, 2019: Performance evaluation of spectral bin classifier (SBC) using ICE-POP 2018 cases. *39th International Conference on Radar Meteorology*, Nara, Japan, September, 1-93.

Bukovcic, P., A. Ryzhkov, D. Zrnic, 2019: Validation of polarimetric relations for snow estimation on radar data. *39th International Conference on Radar Meteorology*, Nara, Japan, September, 3-79.

Carlin, J., and A. Ryzhkov, 2019: Estimation of melting layer cooling rate from dual-polarization radar: spectral bin model simulations. *39th International Conference on Radar Meteorology*, Nara, Japan, September, 2B-04.

Cocks, S., L. Tang, J. Zhang, A. Ryzhkov, P. Zhang, K. Howard, 2019: Enhancing specific attenuation rainfall estimates in stratiform and convective rain regimes. *39th International Conference on Radar Meteorology*, Nara, Japan, September, 10A-1.

Cocks, S., L. Tang, S. Martinaitis, J. Zhang, A. Ryzhkov, P. Zhang, and K. Howard, 2018: A 1 year assessment of four radar based QPE across the continental US. 2019 AMS annual meeting.

Cocks, S., L. Tang, S. Martinaitis, J. Zhang, A. Ryzhkov, P. Zhang, and K. Howard, 2018: Inter-comparisons of radar-based QPE performance for continental, stratiform, and tropical rain regimes. 2019 AMS annual meeting.

French, M. M., J. C. Snyder, K. M. Bedka, and K. M. Calhoun, 2019: Intercomparison between polarimetric radar, GOES-16 satellite, and lightning indicators of storm severity in supercells. *Special Symposium on Meteorological Observations and Instrumentation, 99th Annual Meeting*, Phoenix, AZ, Amer. Meteor. Soc., 817.

French, M. M., D. M. Kingfield, K. S. Tuftedahl, J. H. Segall, J. C. Snyder, 2019: A polarimetric radar climatology of supercell thunderstorms in the United States. *39th International Conf. on Radar Meteorol.*, Nara, Japan. 5B-04.

Hanft, W., J. Zhang, P. Bukovcic, A. Ryzhkov, S. Cocks, S. Martinaitis, K. Howard, 2019: Dual-polarization radar snow QPE in MRMS. *39th International Conference on Radar Meteorology*, Nara, Japan, September, 3-70.

Kim, K., A. Ryzhkov, P. Bukovcic, W. Bang, G. Lee, 2019: Polarimetric retrieval of precipitation rate in cold season using data from ICE-POP 2018. *39th International Conference on Radar Meteorology*, Nara, Japan, September, 3-104.

Lee, G., D. Lee, G. Kim, A. Ryzhkov, G. Lyu, W. Bang, H. Park, 2019: Improved small scale QPE in Seoul metropolitan area by combining X-band and S-band dual-polarimetric radar networks. *39th International Conference on Radar Meteorology*, Nara, Japan, September, 10A-03.

Lee, D., A. Ryzhkov, G. Lyu, C. Lee, W. Bang, H. Park, G. Lee, 2019: Improved QPE by mitigating partial beam blocking in Seoul metropolitan area: Use of radar reflectivity statistics. *39th International Conference on Radar Meteorology*, Nara, Japan, September, 3-90.

Ortega, K. L., K. L. Elmore, and J. C. Snyder, 2019: Using deep learning with polarimetric radar data to predict hail size. *18th Conf. on Artificial and Computational Intelligence and Its Applications to the Environmental Sciences*, *99th Annual Meeting*, Phoenix, AZ, Amer. Meteor. Soc., 2A.3.

Park, H., S. Jung, A. Ryzhkov, D. Yeom, G. Lee, 2019: Improved quantitative precipitation estimation using pseudo KDP by improving spatial continuity. *39th International Conference on Radar Meteorology*, Nara, Japan, September, 3-85.

Schuur, T., E. Griffin, and A. Ryzhkov, 2019: Melting layer ice microphysical processes in winter storms as revealed by quasi-vertical profiles of polarimetric WSR-88D radar data. *39th International Conference on Radar Meteorology*, Nara, Japan, September, 2B-02.

Seo, B.C., W. Krajewski, and A. Ryzhkov, 2018: Multi-year evaluation of the specific attenuation method for quantitative precipitation estimation over Iowa. AGU Annual Meeting, Washington, D.C., December 2018.

Snyder, J. C., J. Krause, and A. Witt, 2019: Developing and assessing the performance of an object-based tornado debris signature detection algorithm. *39th International Conf. on Radar Meteorol.*, Nara, Japan. 2-101.

Snyder, J. C., A. Witt, J. Krause, and K. Ortega, 2019: Polarimetric radar characteristics of large hail and its growth. *39th International Conf. on Radar Meteorol.*, Nara, Japan. 2-102.

Troemel, S., J. Carlin, A. Ryzhkov, and C. Simmer, 2019: Nowcasting of stratiform rain exploiting signatures in the dendritic growth layer, microphysical retrievals and spectral bin modeling. . *39th International Conference on Radar Meteorology*, Nara, Japan, September, 1-68.

Zhang, J., L. Tang, S. Cocks, P. Zhang, A. Ryzhkov, C. Langston, B. Kaney, and K. Howard, 2019: Advantages and challenges of a specific attenuation based radar QPE for operations. *39th International Conference on Radar Meteorology*, Nara, Japan, September, 4B-05.

Additional references

Bukovcic, P., A. Ryzhkov, D. Zrnic, and G. Zhang, 2018: Polarimetric radar relations for quantification of snow based on the disdrometer data. *Journal of Applied Meteorology and Climatology*, **57**, 103 – 120.

Greene, D., and R. Clark, 1972: Vertically integrated liquid water – A new analysis tool. *Mon. Wea. Rev.*, **100**, 548 – 552.

Janiszeski, A., R. Rauber, S. Ellis, G. McFarquhar, and B. Jewett, 2019: Elevated convection and fine-scale frontal circulations within the comma-head of a U.S. East Coast winter cyclone. *J. Appl. Meteor. Climatol.*, under review

Leinonen, J., 2014: High-level interface to T-matrix scattering calculations: Architecture, capabilities, and limitations. *Opt. Express*, **22**, 1655-1660.

Mahale, V., G. Zhang, and M. Xue, 2014: Fuzzy logic classification of S-band polarimetric radar echoes to identify three-body scattering and improve data quality. *J. Appl. Meteor. Climatol*., **53**, 2017 – 2033.

Reeves, H., A. Ryzhkov, and J. Krause, 2016: Discrimination between winter precipitation types based on spectral-bin microphysical modeling. *J. Appl. Meteor. Clim.,* **55**, 1747 – 1761.

Rosenfeld, D., 1987: Objective method for analysis and tracking of convective cells as seen by radar. *J. Atmos. Oceanic Technol*., **4**, *422 – 434.*

Ryzhkov, A., H. Reeves, J. Krause, H. Burcham, 2014: Discrimination between winter precipitation types based on explicit microphysical modeling of melting and refreezing in the polarimetric hydrometeor classification algorithm. Extended abstracts. *8th European Conference on Radar in Meteorology and Hydrology*, Garmisch-Partenkirchen, Germany, MIC.P07.

Ryzhkov, A., P. Bukovcic, A. Murphy, P. Zhang, and G. McFarquhar, 2018: Ice microphysical retrievals using polarimetric radar data. *10th European Conference on Radar in Meteorology and Hydrology*, 1 – 6 July, The Netherlands, # 40. Available online at: projects.knmi.nl/erad2018/ERAD2018_extended_abstract_040.pdf.

Tobin, D., and M. Kumjian, 2017: Polarimetric radar and surface-based precipitation-type observations of ice pellet to freezing rain transitions. *Wea. Forecasting*, **32**, 2065 – 2082.

Troemel, S., A. Ryzhkov, P. Zhang, and C. Simmer, 2014: Investigations of backscatter differential phase in the melting layer. *J. Appl. Meteorol. Clim.* **53**, 2344 – 2359.